The International Journal of Advanced Manufacturing Technology
https://doi.org/10.1007/s00170-026-17560-5

ORIGINAL ARTICLE

Machine learning–driven process parameter optimization in directed energy deposition: a multi-objective framework with experimental validation

Parviz Kahhal[1] · Hong Seok Kim[2] · Mahmoud Moradi[3] · Sang-Hu Park[2]

Received: 28 July 2025 / Accepted: 19 January 2026

Abstract

Optimizing process parameters in laser-based Directed Energy Deposition (DED) remains challenging due to nonlinear interdependencies that influence geometric accuracy and mechanical performance. This study presents a machine learning–driven framework that integrates artificial neural network (ANN) surrogate modeling, evolutionary multi-objective optimization, and multi-method sensitivity analysis to enhance process design and decision-making in DED. The framework is experimentally validated using a 1 kW laser system to deposit Inconel 718 onto stainless steel substrates. Two case studies are conducted: (i) optimization of bead geometry (width and dilution depth), and (ii) multi-layer cube fabrication targeting dimensional accuracy and surface hardness. The ANN model is trained on data generated via Design of Experiments, with its structure optimized using grid search to reduce prediction error and improve generalizability. Parameter influence is quantified through three independent sensitivity analysis methods, enabling transparency and interpretability in model behavior. Results show that laser power strongly influences bead width and build height, while nozzle speed and inter-bead spacing affect dilution and deposition uniformity. The Non-Dominated Sorting Genetic Algorithm II (NSGA-II) identifies Pareto-optimal parameter sets, achieving prediction errors below 5%, including dimensional error under 3% and hardness deviation within 3.5%. Unlike prior ANN–NSGA-II approaches, this study integrates a grid search–optimized ANN and applies three complementary sensitivity methods to enhance model interpretability and parameter insight. The modular and data-optimization and significantly reduces experimental workload, supports explainable optimization, and is generalizable to other additive processes. It provides a scalable and intelligent approach for process parameter design in laser-based additive manufacturing.

Keywords Additive manufacturing · Directed energy deposition · Process optimization · Artificial neural networks · Multi-Objective optimization · Sensitivity analysis

1 Introduction

Additive Manufacturing (AM) has revolutionized modern manufacturing by enabling the fabrication of complex, high-precision components with reduced material waste and production time. Techniques such as Powder Bed Fusion (PBF), Material Extrusion (ME), Directed Energy Deposition (DED), Binder Jetting (BJ), and Vat Photopolymerization (VP) have been widely adopted across industries due to their ability to produce customized, lightweight, and high-performance structures [1, 2]. Directed Energy Deposition (DED) is widely used for repairing high-value components, fabricating large-scale structures, and processing functionally graded materials due to its precise material control and

✉ Parviz Kahhal
parviz.kahhal@waikato.ac.nz

✉ Sang-Hu Park
sanghu@pusan.ac.kr

1 School of Engineering, The University of Waikato, Hamilton 3240, New Zealand

2 School of Mechanical Engineering, Pusan National University, Geumjeong-gu, Busan 46241, Korea

3 Faculty of Education, Arts, Science and Technology, University of Northampton, Northampton NN1 5PH, UK

high deposition rates. However, optimizing DED process parameters remains a challenge because nonlinear interactions between laser power, feed rate, powder flow rate, and interlayer spacing influence dimensional accuracy, microstructure, mechanical properties, and residual stresses. These complexities necessitate systematic and data-efficient approaches for understanding and optimizing DED processes [3–5].

1.1 Challenges in process optimization for DED

DED process performance is governed by strongly coupled parameters—laser power, feed rate, powder flow rate, and interlayer spacing—whose nonlinear interactions directly influence bead geometry, microstructure, and residual stresses [6]. These interactions create competing trade-offs that make systematic optimization difficult. Traditional approaches based on trial-and-error or predefined regression models are costly, time-consuming, and unable to capture the nonlinear parameter dependencies observed in DED, limiting their generalizability and use for reliable process planning [6–8].

Physics-based simulations such as FEA and CFD offer deeper insight but are computationally intensive and sensitive to modeling assumptions, restricting their applicability in real-time or iterative optimization. These limitations motivate the use of machine-learning–based surrogate models that can efficiently approximate complex process behaviors while reducing experimental and computational burden [9, 10].

1.2 Machine learning for process optimization

Machine learning (ML) has emerged as a powerful tool for predictive modeling and process optimization in additive manufacturing (AM), offering data-driven alternatives to physics-based and regression-based approaches [11, 12]. Among ML techniques, artificial neural networks (ANNs) are particularly effective for capturing nonlinear relationships, enabling accurate prediction of bead geometry, dilution, and mechanical responses.

Numerous studies have demonstrated ANN capability across AM applications, including parameter prediction [13], hybrid ANN–PSO and RSM-based optimization [14], multi-criteria decision-making [15], thermal field prediction with significant computational reductions [16], and geometric compensation to improve dimensional accuracy [17]. Recent AI-driven developments in 3D printing have demonstrated that stacking artificial-intelligence frameworks can substantially improve prediction accuracy, reduce printing time, and lower material consumption [18]. Earlier data-driven modeling approaches have also shown strong capability in automatically determining optimal printing parameters [19]. Comprehensive surveys further emphasize that, despite progress in AI-based monitoring and parameter tuning, many existing methods remain application-specific and lack unified, interpretable predictive–optimization frameworks [20, 21]. These insights reinforce the need for integrated and data-efficient approaches, motivating the combined ANN, multi-method sensitivity analysis, and NSGA-II framework proposed in this study.

A key limitation of ANNs in AM applications is their black-box nature, which obscures how individual process parameters influence predicted outcomes [22]. Sensitivity analysis provides a means of addressing this issue by quantifying parameter influence and improving interpretability. Accurate model behavior, however, also depends on appropriate network architecture selection; overly complex networks can lead to overfitting and high computational cost, while overly simple architectures may miss critical nonlinear relationships [23–25]. These challenges highlight the need for structured and interpretable ANN-based approaches, motivating the integration of multi-method sensitivity analysis to enhance transparency, generalization, and confidence in AI-driven AM optimization.

1.3 The role of design of experiments (DOE) in AM optimization

Training ANNs effectively requires datasets that capture sufficient variability across the design space, making Design of Experiments (DOE) essential for structured and efficient sampling. DOE techniques facilitate systematic selection of parameter combinations, reducing unnecessary experiments while improving model generalization. Approaches such as full-factorial and space-filling designs (e.g., Sobol sequences, Latin hypercube) and classical methods like Central Composite Design (CCD) help ensure that key process interactions are represented without bias. Well-designed datasets support accurate surrogate modeling by mitigating overfitting and enhancing the robustness of ANN-based optimization frameworks [26, 27].

1.4 Integrating prediction with multi-objective optimization

ANNs provide accurate predictions of process outcomes but do not inherently support parameter optimization, making their integration with multi-objective strategies essential for AM applications involving competing performance metrics. Single-objective methods are insufficient in cases where improvements in mechanical strength may increase residual stresses or affect dimensional accuracy; therefore, multi-objective optimization (MOO) is required to balance geometric fidelity, mechanical properties, production efficiency, and material usage [28]. MOO techniques generate Pareto fronts that reveal optimal trade-offs, allowing engineers to select solutions according to application-specific priorities.

Recent advancements such as multi-objective Bayesian optimization have demonstrated rapid Pareto-front construction with limited experimental evaluations [29]. Metaheuristic algorithms—including genetic algorithms, particle swarm optimization, and simulated annealing—are widely used for complex multi-objective problems where explicit mathematical models are unavailable. Among these, NSGA-II effectively handles high-dimensional, nonlinear design spaces and has been broadly adopted in AM for balancing conflicting objectives across diverse processes [30–33].

However, most existing NSGA-II applications operate without predictive modeling, limiting their adaptability and computational efficiency. This gap motivates the integration of ANN-based surrogate modeling with NSGA-II to enable faster, more informed decision-making and robust process parameter optimization.

1.5 Research gap and proposed framework

Although multi-objective optimization (MOO) is widely used in AM to balance competing goals such as strength, distortion, deposition efficiency, and material usage, many existing studies still rely on direct experimentation or predefined regression models that struggle to represent the nonlinear and dynamic behavior of AM processes. Approaches based on GRA, RSM, Taguchi, or metaheuristic algorithms have shown value for specific applications [34–39], but they depend on simplified model structures or extensive parameter scanning, limiting adaptability and restricting their ability to generalize across broader processing conditions.

To address these limitations, this study introduces an integrated framework that couples ANN-based surrogate modeling with multi-method sensitivity analysis and NSGA-II evolutionary optimization. The ANN component is tuned through a structured grid search to ensure stable prediction quality, while three complementary sensitivity techniques—Partial Derivative, weights-based, and Profile methods—provide both local and global interpretability of parameter influence. This combination supports data-driven learning of process behavior and enables transparent evaluation of trade-offs across conflicting objectives.

The proposed workflow consists of: (i) ANN architecture tuning to avoid overfitting or underfitting, (ii) multi-method sensitivity analysis to quantify parameter significance with interpretable metrics, and (iii) NSGA-II optimization to generate Pareto-optimal solutions aligned with application-specific priorities. Together, these modules create an explainable and computationally efficient optimization environment for DED process tuning.

Although demonstrated here through two experimental DED case studies, the modular construction of the framework—centered on general principles of surrogate modeling, sensitivity analysis, and multi-objective optimization—suggests potential applicability to other manufacturing processes such as Selective Laser Melting (SLM), welding, and CNC machining. Extending the framework to such processes would require process-specific datasets and additional validation, but its architecture is designed to accommodate different input–output relationships and modeling requirements.

By combining interpretable surrogate modeling with multi-objective evolutionary optimization, the framework advances AI-driven process control in AM, supporting improved precision, repeatability, and informed decision-making in complex manufacturing environments.

2 Methodology

This study develops an integrated neural network-driven multi-objective optimization framework for Directed Energy Deposition (DED). The methodology consists of four key components:

i. Data collection through Design of Experiments (DOE),
ii. Artificial Neural Network (ANN) modeling for process outcome prediction,
iii. Sensitivity analysis using the Partial Derivative (PaD) method, weights-based sensitivity analysis, and the Profile Method, and.
iv. Multi-objective optimization using the Non-Dominated Sorting Genetic Algorithm II (NSGA-II).

The framework analyzes key DED process parameters, including laser power (LP), nozzle speed (NS), interlayer bead spacing (IBS), and powder feed rate (PFR), to identify optimal trade-offs among multiple performance objectives such as bead width, dilution depth, cube height, and hardness. Two experimental case studies—single-bead fabrication and cube fabrication—validate the proposed framework, demonstrating its effectiveness in optimizing geometric and mechanical properties in AM.

2.1 Design of experiments (DOE)

Data for model development were generated using structured Design of Experiments (DOE) strategies tailored to the objectives of this study outputs [26, 40]. The DOE provides the datasets required for training surrogate models and supporting subsequent sensitivity analysis and multi-objective optimization.

This study employs two experimental case studies, each using a different DOE strategy to systematically vary key input parameters of the Directed Energy Deposition (DED) process. The first case study follows a full factorial design to capture primary parameter interactions, while the second case study integrates a space-filling Sobol sequence with a Central Composite Design (CCD) to ensure broad coverage of the design space and to support surrogate-based modeling [41, 42]. Detailed experimental configurations and DOE specifications for each case study are provided in the corresponding case-study sections.

2.2 Optimizing ANN architecture for additive manufacturing

Artificial Neural Networks (ANNs) based on the Multi-Layer Perceptron (MLP) architecture were employed as surrogate models to capture the nonlinear relationships between DED process parameters and corresponding process outcomes [43]. In this study, the ANN maps a vector of process inputs to predicted responses such as bead width and dilution depth.

A schematic of the adopted MLP architecture is shown in Fig. 1, illustrating the fully connected structure between the input, hidden, and output layers. For a single-hidden-layer network, the ANN model can be expressed as:

$$\mathbf{y} = f\left(\mathbf{W}_{ho} \cdot \sigma\left(\mathbf{W}_{ih} \cdot \mathbf{x} + \mathbf{b}_1\right) + \mathbf{b}_2\right) \tag{1}$$

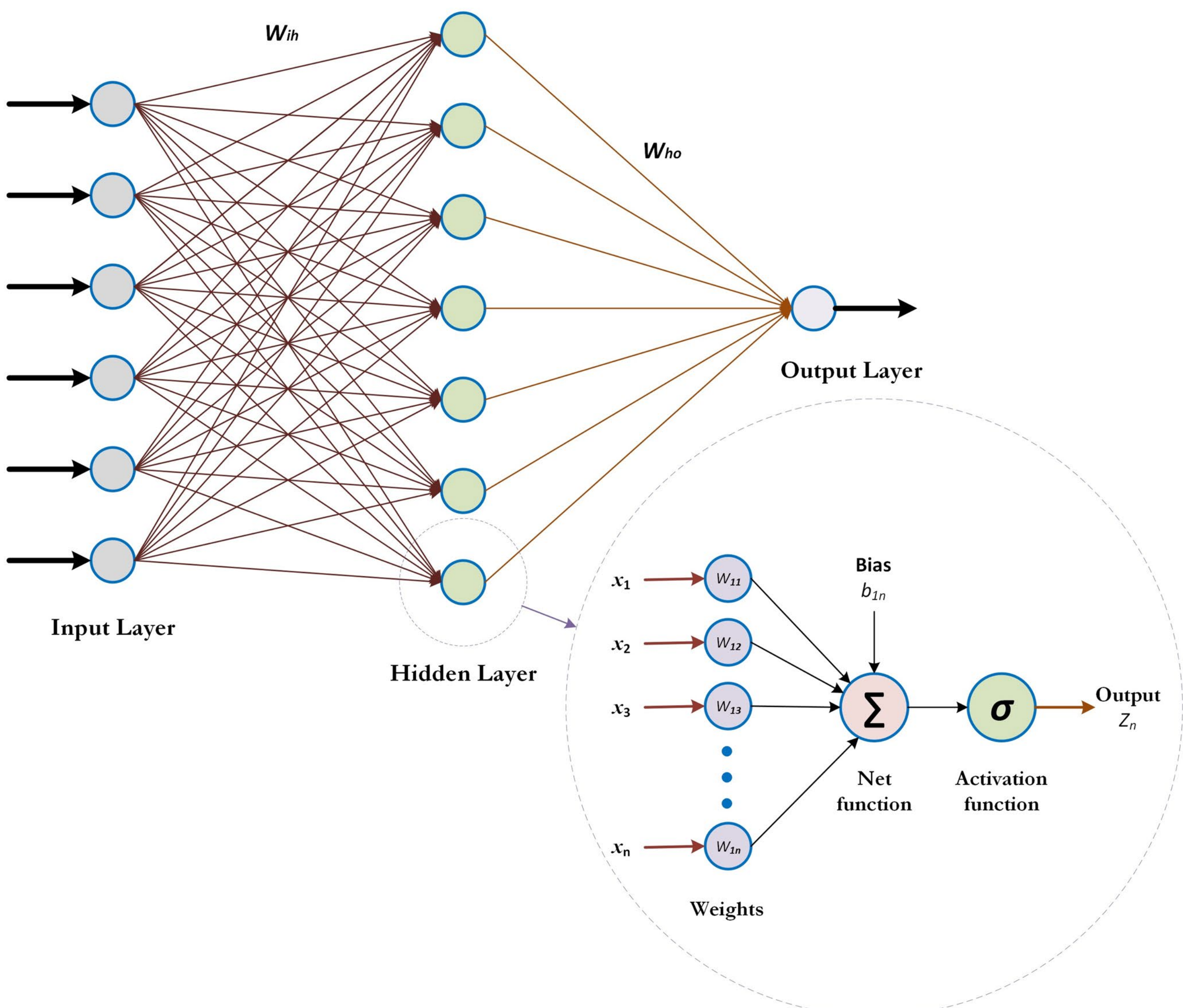

Fig. 1 Schematic representation of an ANN Multi-Layer Perceptron (MLP) showing input, hidden, and output layers with weighted connections

Where $\mathbf{x}$ is the input vector, $\mathbf{W}_{ho}$ and $\mathbf{W}_{ih}$ denote the weight matrices of the hidden and output layers, respectively, $\mathbf{b}_1$ and $\mathbf{b}_2$ are the corresponding bias terms, and $\sigma(\cdot)$ represents the activation function. In this work, a hyperbolic tangent sigmoid activation function was used in the hidden layer:

$$\sigma(z) = \frac{2}{1 + e^{-2z}} - 1 \tag{2}$$

The network output y corresponds to the predicted process response. Model training was performed by minimizing the Mean Squared Error (MSE) between predicted and experimental values:

$$\mathrm{MSE} = \frac{1}{n}\sum{}_{i=1}^{n}(y_i - \widehat{y}_i)^2 \tag{3}$$

where y_i and $\widehat{y}_i$ denote the experimental and ANN-predicted responses, respectively. Weight updates were obtained through iterative optimization during training to achieve convergence of the prediction error. Minimization of the MSE was carried out using the Levenberg–Marquardt optimization algorithm, which iteratively updates the network weights to achieve convergence of the prediction error.

2.2.1 Balancing model complexity: overfitting vs. Underfitting

Achieving an optimal ANN architecture requires balancing model complexity to prevent overfitting and underfitting [44]. Overfitting occurs when the model is too complex, capturing noise along with meaningful patterns, leading to poor generalization. Underfitting, in contrast, results from an overly simplistic model that fails to capture key relationships, reducing performance on both training and testing data.

To address this, a grid-search strategy was employed to systematically evaluate the effect of the number of layers and neurons on surrogate-model accuracy. Multiple ANN configurations were trained and compared using the Root Mean Squared Error (RMSE) on the training (70%), validation (15%), and testing (15%) subsets. This ensured that the final ANN model maintained sufficient representational capacity while avoiding unnecessary complexity.

Figure 2 presents the ANN optimization flowchart, illustrating the network-selection process from data preprocessing to final model evaluation. A Monte-Carlo resampling–based optimization framework was implemented to enhance robustness in the small-data regime. For each of approximately 1500 independent training runs, the dataset was normalized using *mapminmax* and randomly divided into training, validation, and test subsets (70/15/15). The hyperparameter search space included 1–3 hidden layers and 1–12 neurons per layer, with a hyperbolic tangent sigmoid (*tansig*) activation function in the hidden layers and *purelin* in the output layer. Training was carried out using the Levenberg–Marquardt algorithm (*trainlm*) with validation-based early stopping (maximum six validation checks). Each run began from a new random initialization.

A model was accepted as the new best architecture only when all major performance metrics (RMSE, R, and R^2

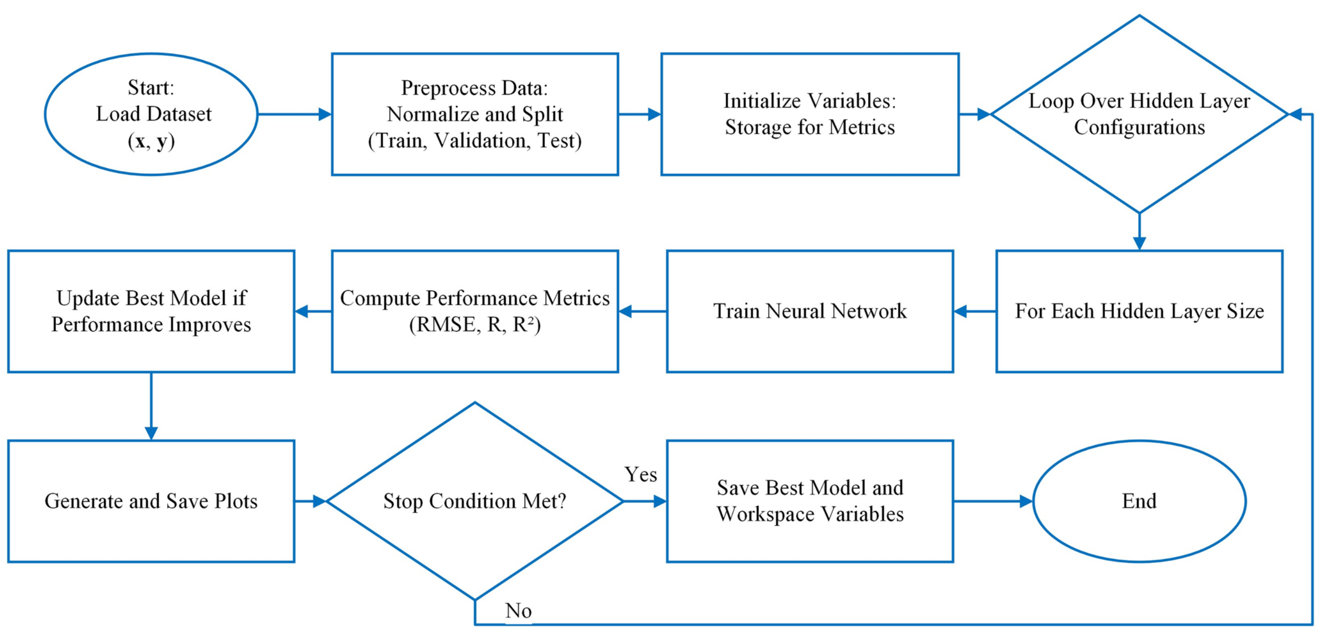

Fig. 2 ANN Optimization Flowchart representing the process of optimizing the neural network architecture through grid search, evaluating performance, and selecting the best model

across training, validation, and test sets) improved simultaneously. This strict multi-metric selection rule ensures that the final surrogate model is not dependent on any single data partition but instead represents the most stable and statistically reliable network identified across extensive randomized resampling.

All ANN preprocessing steps, input–output normalization procedures, randomized data partitioning, hyperparameter search ranges, random initialization protocols, and model-selection criteria are detailed in the subsequent ANN methodology subsection.

2.3 Multi-Objective optimization using NSGA-II

To identify optimal trade-offs among competing performance objectives in the Directed Energy Deposition (DED) process, this study employs the Non-Dominated Sorting Genetic Algorithm II (NSGA-II), a widely used evolutionary algorithm for multi-objective optimization [45]. Population-based evolutionary optimizers such as NSGA-II are well suited for complex manufacturing problems due to their ability to efficiently explore nonlinear, high-dimensional design spaces without requiring gradient information [46, 47].

In the proposed framework, NSGA-II is integrated with trained Artificial Neural Network (ANN) surrogate models, which provide rapid predictions of process responses for candidate parameter sets. This surrogate-assisted strategy enables efficient exploration of the design space while avoiding additional experimental trials or computationally expensive physics-based simulations. All objectives were formulated within a consistent minimization framework; objectives originally defined as maximization goals were converted by sign inversion. Objective values were handled directly by the solver, as their numerical scales were comparable within each case study.

NSGA-II applies an elitist non-dominated sorting strategy to rank candidate solutions according to Pareto dominance, while solution diversity is preserved using a crowding-distance mechanism [30]. A solution is considered Pareto optimal if it is no worse than any other solution across all objectives and strictly better in at least one objective [48]. Through this mechanism, NSGA-II generates a set of non-dominated solutions that represent trade-offs among conflicting objectives rather than a single optimal point.

During each iteration, parent and offspring populations are combined and ranked, and the next generation is constructed by prioritizing solutions with superior dominance rank and greater crowding distance. Genetic operators, including crossover and mutation, are applied to generate new candidate solutions, and the process is repeated until the predefined termination criteria are met. The resulting Pareto front provides a structured representation of achievable trade-offs, enabling informed selection of process parameters according to application-specific [49, 50].

Figure 3 presents a schematic overview of the NSGA-II workflow adopted in this study, illustrating the iterative population initialization, surrogate-based fitness evaluation, non-dominated sorting, diversity preservation, and Pareto-front generation steps [51]. Detailed solver configurations, convergence behavior, and multi-run stability analyses are reported separately for each experimental case study in Sect. 4.1.4 and 4.2.4.

2.4 Sensitivity analysis

To better understand the influence of process parameters, sensitivity analysis was conducted using three methods: the Partial Derivative (PaD) method, weights-based sensitivity analysis, and the Profile Method. Each method quantifies the impact of input variables on Artificial Neural Network (ANN) predictions, offering insights into parameter significance and model behavior.

2.4.1 Partial derivative method (PaD)

The Partial Derivative (PaD) method quantifies how changes in each input parameter affect ANN outputs by computing first-order partial derivatives. This technique provides an analytical measure of parameter influence, making it useful for interpreting the internal mechanisms of ANN models [22, 52].

For a feedforward neural network with J input neurons, H hidden neurons, and one output neuron, the sensitivity S_j of the output y with respect to the input x_j is computed as:

$$S_j = \frac{\partial y}{\partial xj} = \sum {}_{h=1}^{H} W_{oh} \cdot \sigma' (z_h) \cdot W_{hj} \tag{4}$$

where:

- W_{oh} is the weight from hidden neuron h to the output.
- W_{hj} is the weight from input x_j to hidden neuron h, and.
- $\sigma' (zh)$ is the derivative of the activation function, given for the hyperbolic tangent sigmoid function as:

$$\sigma' (z_h) = 1 - a_h^2, \quad a_h = \tanh\left(b_h + \sum {}_{j=1}^{J} W_{hj} \cdot x_j\right) \tag{5}$$

- b_h is the bias term of the hidden neuron.

The total contribution of each input is quantified using the Sum of Squared Derivatives (SSD):

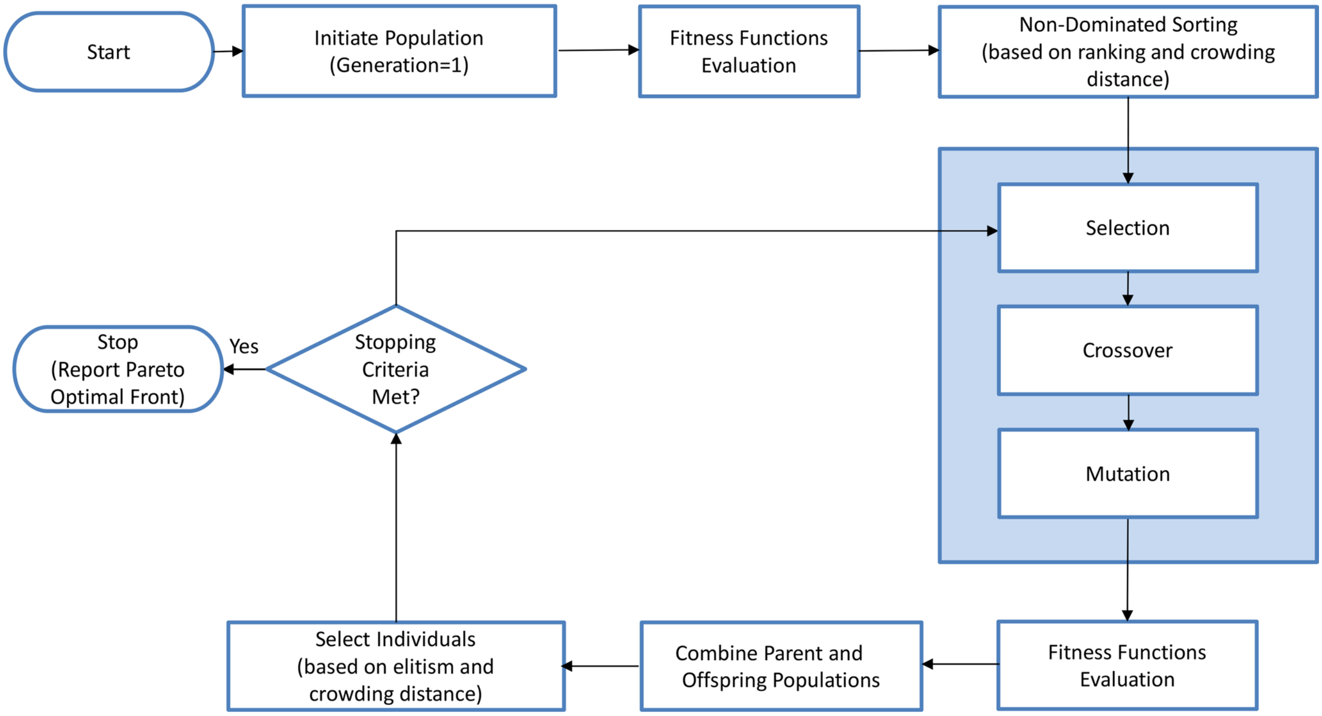

Fig. 3 Schematic representation of the NSGA-II procedure used for Pareto-front generation in the proposed optimization framework

$$SSD_j = \sum {}_{n=1}^{N}\left(\frac{\partial y}{\partial xj}\right)_n^2 \tag{6}$$

Where SSD_j represents the cumulative sensitivity of input x_j across N samples. In this study, partial derivatives are evaluated in the normalized input space, and SSD aggregation provides a magnitude-based measure of sensitivity, thereby removing sign information. A higher SSD_j value indicates greater influence of the input variable on ANN predictions.

The PaD method enhances ANN interpretability by ranking input importance based on connection weights and activation behavior, making it particularly effective for complex, nonlinear models [22]. While local derivative signs can indicate directional trends, SSD-based rankings are primarily used here to assess relative parameter importance, which is appropriate for nonlinear systems with varying local sensitivities [52]. In this study, PaD-based sensitivity rankings are used to identify dominant process parameters, with their statistical behavior and stability examined in the corresponding case studies.

2.4.2 Weights-Based sensitivity analysis

The weights-based sensitivity analysis determines the relative importance (RI) of input variables in an ANN by evaluating the absolute magnitudes of connection weights across layers. This method considers both input-to-hidden and hidden-to-output weight contributions, ensuring a comprehensive assessment of variable significance [53].

The weights-based sensitivity analysis follows a three-stage process to determine the relative importance of input variables in an ANN. In the first stage, the contribution of each input is computed by multiplying the absolute values of the input-to-hidden layer weights with the corresponding hidden-to-output layer weights:

$$P_{ih} = |W_{ih}| \cdot \ |W_{ho}| \tag{7}$$

where P_{ih} represents the weighted contribution of input i through hidden neuron h.

In the second stage, these weighted contributions are normalized to ensure comparability across neurons:

$$Q_{ih} = \frac{P_{ih}}{\sum {}_{j=1}^{n} P_{jh}} \tag{8}$$

In the final stage, the relative importance (RI) of each input is determined by aggregating the normalized contributions across all hidden neurons:

$$RI_i = \frac{\sum {}_{h=1}^{H} Q_{ih}}{\sum {}_{h=1}^{H} \sum {}_{i=1}^{n} Q_{ih}} \times 100 \tag{9}$$

where RI_i represents the percentage contribution of input i to the ANN output. The use of absolute weights avoids sign cancellation effects, and the stability of the resulting rankings is examined through cross-method comparison in Sect. 2.4.4. The weights-based method provides a complementary, architecture-level view of input importance, and its consistency with other sensitivity measures is evaluated in the case studies.

2.4.3 Profile method

The Profile Method systematically evaluates the sensitivity of input variables in an ANN while holding all other inputs constant at predefined levels [54]. Unlike weight-based methods, this approach directly examines the effect of parameter variations while considering nonlinear interactions.

Each input variable is divided into equal intervals (referred to as the scale) spanning its minimum to maximum values. To account for interaction effects, all remaining variables are fixed at five reference levels: minimum, first quartile (25%), median (50%), third quartile (75%), and maximum. The ANN output is computed for each scale level, and the median response across the five conditions is recorded to form a profile curve [22] (Fig. 4).

The contribution C_i of input variable i is computed as:

$$C_i = \frac{max\,(Y_i) - min\,(Y_i)}{\sum_{j=1}^{n} (max\,(Y_j) - min\,(Y_j))} \times 100 \tag{10}$$

where Y_i represents the ANN outputs obtained when varying input $_i$ across its scale while keeping other variables fixed. $max(Y_i)$ and $min(Y_i)$ denote the maximum and minimum ANN output values for input i.

Multiple scales (12, 24, 48, 96, 144, and 192) were tested, and convergence was assessed based on the stability of sensitivity rankings across increasing resolutions. The Profile Method is particularly valuable for analyzing nonlinear interactions and capturing variable importance in complex ANN models, while detailed interaction analyses are presented in the corresponding case studies.

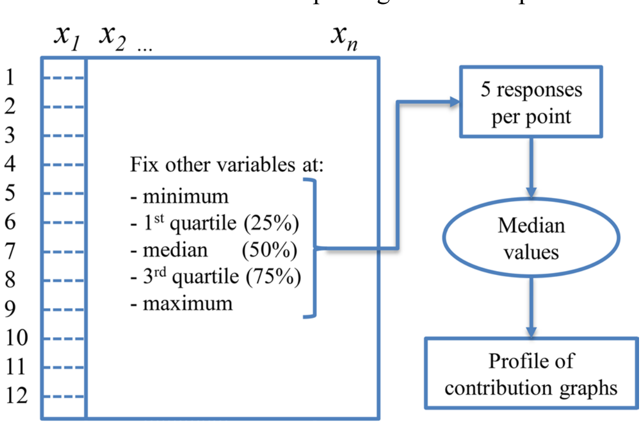

Fig. 4 Simplified representation of the Profile Method, illustrating the process of systematically varying one input while keeping others fixed at predefined levels to generate contribution profiles

2.4.4 Cross-Method consistency and Rank-Correlation analysis

To evaluate the robustness of the sensitivity analysis, the rankings obtained from the PaD, weights-based, and profile methods were compared using non-parametric rank-correlation metrics. Agreement among these independent techniques supports the conclusion that the identified parameter hierarchies are not artifacts of any single sensitivity definition.

Rank similarity was assessed using Spearman's rank correlation coefficient (ρ) and Kendall's rank coefficient (τ) [55, 56]. For two ranked variables $R_x$and R_y, Spearman's ρ is defined as:

$$\rho = 1 - \frac{6\sum_{i=1}^{n}(R_{x,i} - R_{y,i})^2}{n(n^2 - 1)} \tag{11}$$

Kendall's τ evaluates the agreement based on the number of concordant (C) and discordant (D) pairs:

$$\tau = \frac{C - D}{\frac{1}{2}n(n-1)} \tag{12}$$

Both coefficients range from −1 (perfect disagreement) to +1 (perfect agreement), with values near +1 indicating strong consistency in parameter rankings across the three sensitivity methods.

2.5 Architecture and generalizability of the framework

The proposed optimization framework is designed with a modular and scalable architecture that enables seamless integration of data-driven modeling, interpretability mechanisms, and evolutionary optimization. The core components—artificial neural networks (ANNs), sensitivity analysis, and NSGA-II—are independently structured, allowing for flexibility in model replacement or extension. For instance, while an ANN-based surrogate model is used in this study, the structure supports alternative machine learning models (e.g., decision trees, Gaussian processes) as needed.

The incorporation of three complementary sensitivity analysis methods (partial derivatives, weights-based, and profile method) not only improves transparency but also allows users to interpret the contribution of each input variable, building trust in the model's predictions. This interpretability is particularly important in high-stakes industrial settings, where decision-making must be guided by understandable and verifiable data.

Although the framework is validated through two case studies in laser-based Directed Energy Deposition (DED), it is intentionally designed to be generalizable to other advanced manufacturing domains. These include Powder Bed Fusion (PBF), Selective Laser Melting (SLM), Electron Beam Melting (EBM), welding, and even subtractive processes like CNC machining. The surrogate-optimizer combination is equally applicable in any setting where nonlinear, multi-objective parameter tuning is required.

Overall, the framework serves as a practical and explainable AI tool that supports informed decision-making across a range of manufacturing systems, reducing the need for exhaustive trial-and-error experimentation and enabling faster convergence to optimal processing conditions.

2.6 Implementation

The entire methodology was implemented in MATLAB (R2020b), utilizing the Global Optimization Toolbox for multi-objective optimization with NSGA-II and standard neural network functions for ANN modeling. The Design of Experiments (DOE) was carried out using the Model-Based Calibration (MBC) Model, enabling systematic and data-efficient exploration of the design space. All simulations were executed on a workstation equipped with 12 CPU cores and 32 GB RAM, running Windows 10.

For ANN implementation, hyperbolic tangent sigmoid (*tansig*) activation functions were employed in all hidden layers, while a linear (*purelin*) activation function was used in the output layer. This configuration is well suited for regression tasks and ensures unbiased reconstruction of continuous physical quantities after inverse normalization of the network outputs.

MATLAB scripts were developed to perform ANN architecture optimization, sensitivity analysis (partial derivative, weights-based, and profile methods), and evolutionary multi-objective optimization. Case-specific solver parameters, random initialization protocols, and validation procedures are reported in the corresponding experimental case-study sections.

Accordingly, this work is positioned as an integrated predict–optimize–interpret framework rather than a surrogate benchmarking study, with the ANN serving as an effective representative surrogate model.

3 Experimental case studies

To validate the neural network-driven multi-objective optimization framework developed in this study, two experimental case studies were conducted. The first case study focuses on single-bead fabrication, where the objectives are to control width of bead and depth of dilution. The second case study focuses on cube fabrication, where the primary objectives are to optimize the height of cube and hardness. These experiments were performed using Directed Energy Deposition (DED) with a range of process parameters, and the results were used to assess the performance of the optimization framework.

3.1 Directed energy deposition (DED) process

Directed Energy Deposition (DED) is a useful additive manufacturing (AM) technique that employs focused thermal energy, such as a laser beam, to melt and deposit material layer by layer. This study utilized the DED process to experimentally validate the proposed neural network-driven multi-objective optimization framework. By utilizing the DED process, the framework was assessed for its ability to optimize critical geometric and material properties in additive manufacturing.

3.1.1 Materials and equipment

In the experiments, Inconel 718 powder was deposited onto a Grade SUS 316 L stainless steel (STS 316 L) substrate. Inconel 718 is a nickel-based superalloy widely used for its high-temperature strength and corrosion resistance, while STS 316 L is commonly adopted in DED due to its durable metallurgical compatibility with Ni-based alloys [40, 57].

The Inconel 718 feedstock used in this study was supplied as Sandvik Osprey® 718, a gas-atomized powder designed specifically for additive manufacturing. According to the supplier datasheet, the powder exhibits spherical morphology, low oxygen levels, low inclusion content, and good flowability, all of which are essential for stable melt-pool behavior during DED. The supplied particle size distribution was −150+45 μm, which falls within Sandvik's standard DED feedstock specification (typically 53–150 μm) and is consistent with the operational PSD range used in this study. Batch-specific D10/D50/D90 values were not provided; however, the powder was manufactured under tightly controlled gas-atomization conditions that ensure uniform particle distribution and morphology.

The nominal chemical composition of Sandvik Osprey® 718 (wt%) is provided in Table 1 [58].

Table 1 Chemical composition of Sandvik osprey inconel 718 powder (wt%)

Element	Ni	Cr	Nb	*P*	Ti	Al	S	Mo
wt%	50.0–55.0	17.0–21.0	4.75–5.50	≤0.015	0.65–1.15	0.20–0.80	≤0.015	2.80–3.30
Element	**Co**	**Mn**	**Si**	**C**	**Fe**	**B**	**Cu**	
wt%	≤1.00	≤0.35	≤0.35	≤0.08	Bal.	≤0.006	≤0.30	

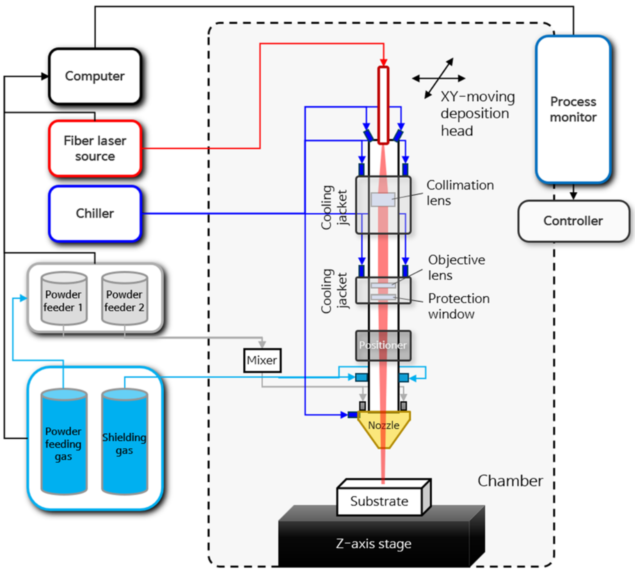

Fig. 5 Schematic of the Directed Energy Deposition (DED) process

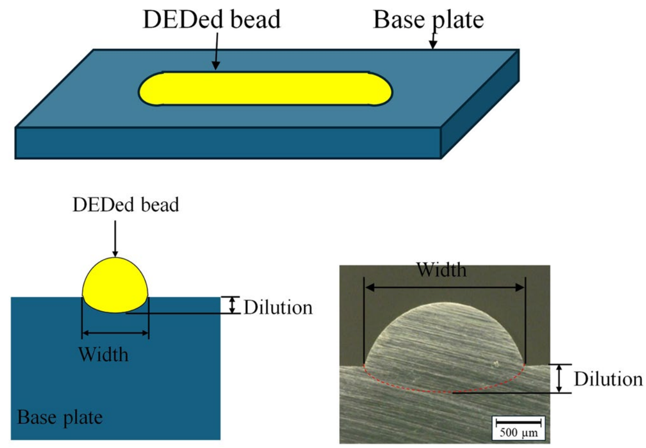

Fig. 6 Dilution depth and width of the single bead

All powder handling followed the laboratory's standard operating procedures, including storage in sealed containers and argon shielding during deposition.

The DED process utilized a 1 kW fiber laser (RFL-C1000, Raycus, China) integrated into a coaxial deposition head with a focal spot diameter of approximately 1 mm. An XY-axis moving deposition head combined with a Z-axis stage ensured accurate positioning of both the laser and powder stream. Argon gas was employed as both carrier and shielding gas to minimize oxidation and maintain a low-oxygen deposition environment.

Prior to deposition, the STS 316 L substrate was cleaned with acetone; no intentional pre-heating was applied.

3.1.2 DED mechanism

Figure 5 provides a schematic representation of the DED mechanism. In this process, the laser beam fuses the base material and powder to create a melt pool, where the material solidifies upon cooling to form the desired structure. Successive layers are added with a controlled thickness, enabling the construction of complex geometries. The precise control over energy input, material feed, and process parameters makes DED a suitable method for achieving specific objectives in advanced manufacturing.

3.2 Case study 1: Single-Bead fabrication

This experiment focuses on optimizing bead geometry—specifically the width of bead—and assessing depth of dilution in single-bead Directed Energy Deposition (DED). Width of bead defines the lateral spread of the deposited material, influencing dimensional accuracy, resolution, and material efficiency. Depth of dilution, on the other hand, quantifies the extent of penetration into the substrate, ensuring strong metallurgical bonding and uniform material properties between the deposited layer and the base material [59]. Both attributes directly affect the mechanical properties and overall quality of the deposited part.

The optimization considers three key process variables: laser power (LP), nozzle speed or feed rate (NS), and powder feed rate (PFR). As illustrated in Fig. 6, the width of bead defines the lateral spread of the deposited material, influencing dimensional accuracy and material efficiency, while depth of dilution quantifies substrate penetration, affecting bonding and interfacial properties.

3.2.1 Experimental setup and problem definition

The experiments were performed using a DED machine equipped with a laser power range of 200 W to 500 W, a nozzle speed (feed rate) of 400 mm/min to 700 mm/min, and a powder feed rate of 4 g/min to 8 g/min. The non-linear optimization problem can be represented in the following form:

Objective 1: Width of Bead

- Goal: 1000 μm
- Objective Function to be minimized:

$$Obj_w = |W - 1000| \tag{13}$$

- W: Width of Bead

Objective 2: Depth of Dilution

- Goal: Maximization
- Objective Function to be maximized:

$$Obj_D = D \tag{14}$$

- D: Depth of Dilution

Subject to:

$$\begin{array}{r} 200 \leq \ LP \leq \ 400 \\ 500 \leq \ NS \leq \ 700 \\ 4 \leq \ PFR \leq \ 8 \end{array} \tag{15}$$

- LP: Laser Power (W)
- NS: Nozzle Speed (mm/min)
- PFR: Powder Feed Rate (g/min)

Figure 7 illustrates the steps involved in the Single-Bead Fabrication experiments and the measurement of objective functions.

The single-bead experiments were designed using a full factorial Design of Experiments (DOE) to systematically evaluate the effects of laser power (LP), nozzle speed (NS), and powder feed rate (PFR) on bead geometry. Each factor was varied at three discrete levels, resulting in a 3^3full factorial design comprising 27 unique parameter combinations, thereby covering all possible combinations within the selected parameter ranges. Laser power was varied at 200, 300, and 400 W; nozzle speed at 500, 600, and 700 mm/min; and powder feed rate at 4, 6, and 8 g/min. This design enabled comprehensive assessment of both main effects and interaction effects, with the center-point condition (LP=300 W, NS=600 mm/min, PFR=6 g/min) naturally included within the design space.

For each experimental trial, the width of bead and depth of dilution were quantified through cross-sectional analysis of optical microscopy (OM) images acquired using an Axiolab 5 microscope (Zeiss, Germany). All experimental runs were executed in randomized order to mitigate systematic bias. No blocking was applied, as all experiments were conducted under identical machine and environmental conditions. Fixed auxiliary parameters included a coaxial shielding gas flow rate of 6 L/min and a powder feeding gas flow rate of 3.5 L/min, both using argon. Three-dimensional and pairwise projections of the investigated process parameters are presented in Fig. 8, and the complete DOE matrix for the single-bead case study, including factor definitions and units, is provided in Supplementary Table S1.

3.3 Case study 2: cube fabrication

The second experimental case study focuses on cube fabrication, where the objectives were to optimize height of cube and material hardness. Height of cube is critical for ensuring dimensional accuracy, while hardness directly affects the mechanical properties of the fabricated part. The optimization considers three key process variables: laser power

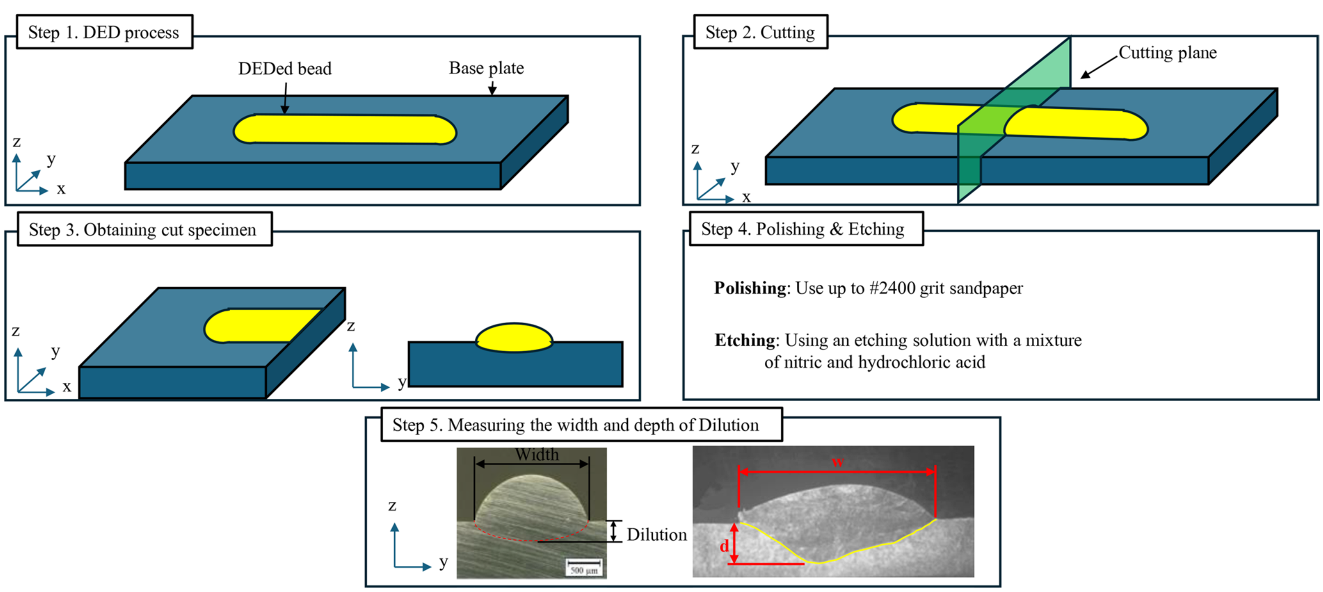

Fig. 7 Steps of Single-Bead Fabrication experiments and measurement of objective functions (width of bead and depth of dilution)

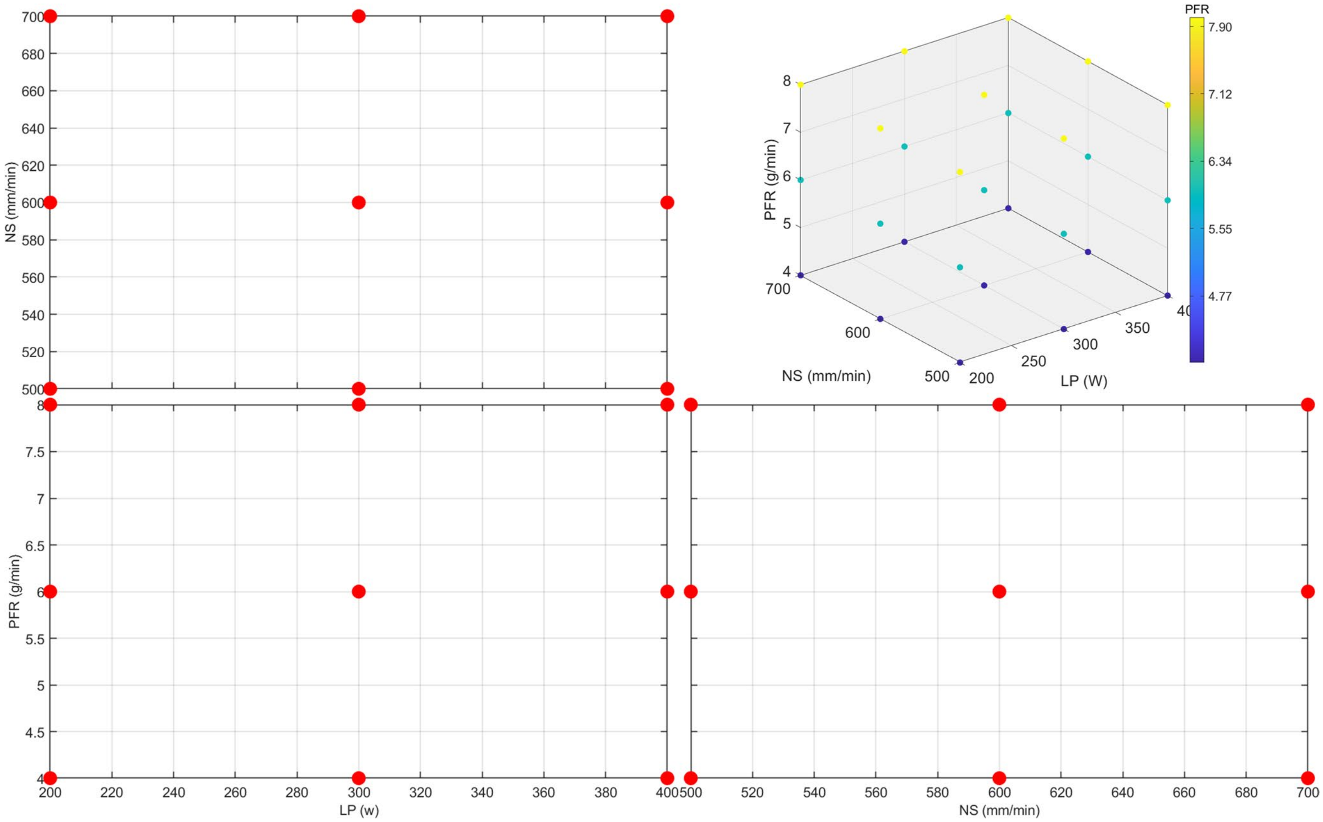

Fig. 8 3D and Pairwise projection of variables (Full factorial design)

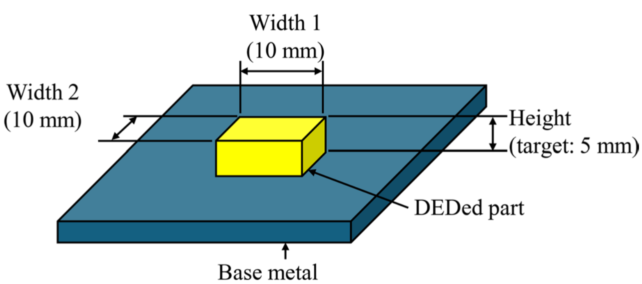

Fig. 9 Schematic of the cube

(LP), nozzle speed or feed rate (NS), and inter-bead spacing (IBS). Figure 9 illustrates the schematic of the cube.

3.3.1 Experimental setup and problem definition

The experiments were performed using a DED machine equipped with a laser power range of 100 W to 500 W, a nozzle speed (feed rate) of 500 mm/min to 900 mm/min, and inter-bead spacing (IBS) from 0.1 mm to 0.9 mm. This spacing directly controlled the overlap between deposition tracks during cube fabrication. A smaller IBS value resulted in greater overlap, which helped ensure sufficient bonding between adjacent tracks and consistent layer buildup. In contrast, a larger IBS reduced the overlap, potentially leading to weak bonding or surface defects. Managing track overlap was critical for achieving the target cube height and uniform hardness. The non-linear optimization problem can be represented in the following form:

Objective 1: Height of cube

- Goal: 5 mm
- Objective Function to be minimized:

$$Obj_{H1} = |H_1 - 5| \tag{16}$$

- H_1: Height of cube.

Objective 2: Hardness

- Goal: Maximization
- Objective Function to be maximized:

$$Obj_{H2} = mean\,(H_2) \tag{17}$$

- H_2: Average Hardness Measured at Five Points

Subject to:

$$\begin{array}{l} 100 \le LP \le 500 \\ 500 \le NS \le 900 \\ 0.1 \le IBS \le 0.9 \end{array} \tag{18}$$

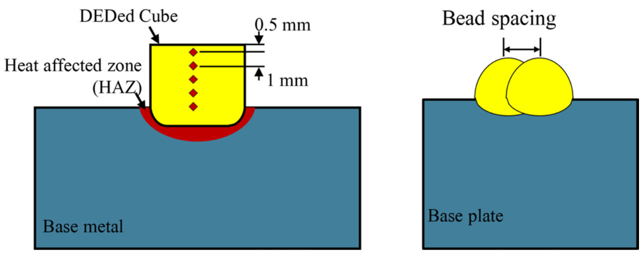

Fig. 10 Cube fabrication objective functions schematics

.

- *LP*: Laser Power (W)
- *NS*: Feed Rate or Nozzle Speed (mm/min)
- *IBS*: Inter-Bead Spacing (mm)

Based on the experimental design space, the linear energy density ranged from 0.11 to 1.00 J/mm, while the areal energy density varied between 0.12 and 1.25 J/mm². The focal spot diameter was approximately 1 mm. Inter-bead spacing (IBS) directly governed track overlap, which ranged from 25% to 90% depending on the measured bead width. Cube fabrication was performed by depositing discrete, parallel beads without a continuous raster scan; IBS therefore defines the effective spacing and overlap between adjacent tracks in each layer.

Figure 10 shows the objective functions schematics.

Figure 11 outlines the steps involved in the Cube Fabrication experiments and the measurement of objective functions. The height measurements were performed using a BLUETEC Height Gauge, while hardness measurements were conducted using the HM-112 micro Vickers hardness tester from Mitutoyo, Japan.

To ensure repeatability and traceability, the height and hardness measurements followed a standardized procedure. Height was recorded using the BLUETEC digital gauge with a resolution of ±0.01 mm, and five measurements were taken at different surface locations; the mean value was used as the response H_1. Hardness testing was carried out according to ASTM E384 using a 300 gf load and 10 s dwell time. After metallographic polishing, five Vickers indentations were placed along the vertical centerline of the cube with a minimum spacing of three times the indent diagonal to avoid interaction of plastic zones. Indentation locations were selected to avoid the melt-pool boundary and heat-affected zone, ensuring that the measurement reflected bulk material properties. The average hardness value H_2 was computed from the five indentations, and the instrument repeatability was within ±5 HV. Figure 11 illustrates the specimen fabrication workflow and the measurement procedures for cube height and hardness.

The cube fabrication experiments were designed using a hybrid Design of Experiments (DOE) that combines a space-filling Sobol sequence with a classical Central Composite Design (CCD), as introduced in Sect. 2.1. The design space was defined as 100 ≤ laser power (LP) ≤ 500 W, 500 ≤ nozzle speed (NS) ≤ 900 mm/min, and 0.1 ≤ inter-bead spacing (IBS) ≤ 0.9. Space-filling Sobol low-discrepancy sequences were first employed to generate sampling points uniformly distributed within the interior of the design space, ensuring broad coverage and robust surrogate-model training under a limited experimental budget, while reducing the risk of overlooking critical regions [42].

To complement the global exploration provided by the Sobol sequence and to enable accurate modeling of local curvature and interaction effects, a rotatable Central Composite

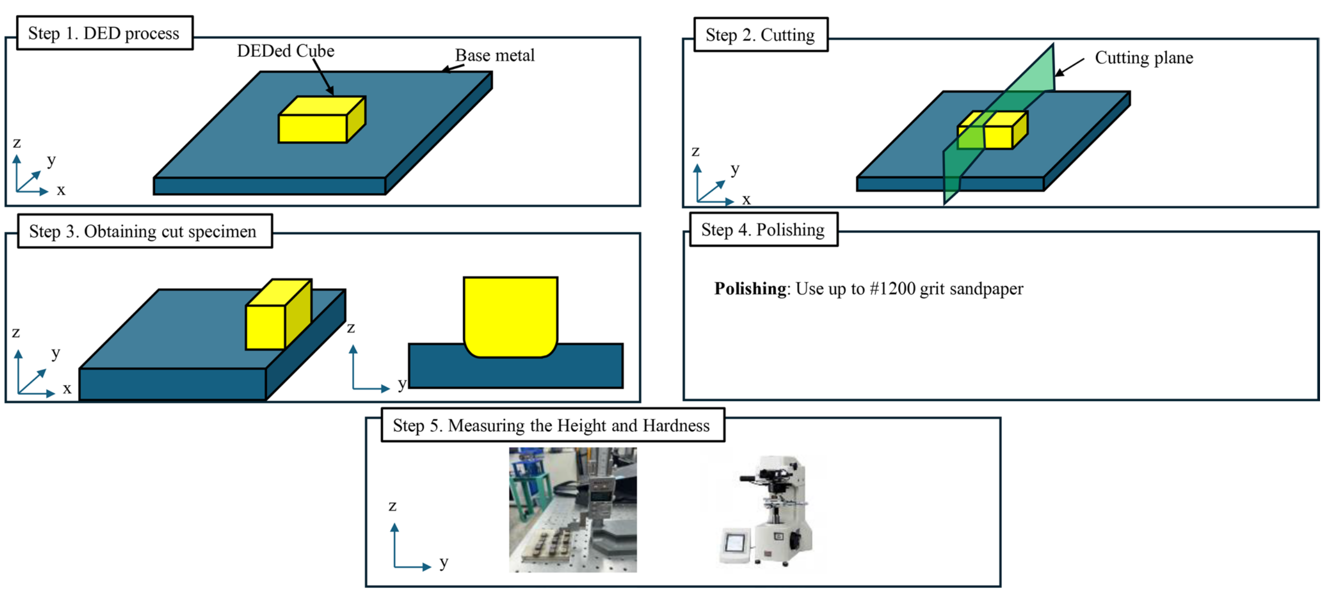

Fig. 11 Steps of Cube Fabrication experiments and measurement of objective

Design (CCD) was embedded within the same design space [41]. The CCD included one center point at (LP = 300 W, NS = 700 mm/min, IBS = 0.5) and six axial points located at ± α along each factor axis, where α ≈ 1.682. These axial points correspond to LP = 131.8/468.2 W, NS = 531.8/868.2 mm/min, and IBS = 0.1636/0.8364, enabling estimation of second-order effects without excessive experimental runs.

In total, the hybrid Sobol–CCD DOE comprised 35 experimental trials, including Sobol sequence points, CCD axial points, and the center point. All experiments were executed in randomized order to mitigate systematic bias. For each trial, cube height and hardness were measured under fixed processing conditions, including coaxial shielding gas (Argon) at 4 L/min, feeding gas (Argon) at 7 L/min, powder feed rate fixed at 4.7 g/min, and a Z-pitch of 0.25 mm. The complete DOE matrix and corresponding measured responses, including factor definitions and units, are provided in Supplementary Table S2.

Figure 12 presents the three-dimensional and pairwise projections of the experimental points, confirming that the combined Sobol–CCD strategy achieves both global space-filling coverage and local curvature resolution, which is essential for accurate surrogate modeling and subsequent multi-objective optimization.

4 Results and discussion

This section presents the experimental results from the two case studies: single-bead fabrication and cube fabrication. The discussion covers the ANN model's predictive accuracy, sensitivity analysis, and the Pareto optimization results for each case.

4.1 Case study 1: Single-Bead fabrication

4.1.1 Experimental results

The experiments were conducted using a full-factorial Design of Experiments (DOE) approach, systematically varying laser power, feed rate, and powder feed rate across 27 trials. For each fabricated bead, width and dilution depth were evaluated using image-analysis software, with measurements repeated several times on the same cross-section to account for measurement noise and ensure consistency. The mean of these repeated measurements was used as the reported value.

The cross-sectional and surface view of one of the fabricated beads (No. 20) is shown in Fig. 13, including width of bead and depth of dilution, highlighted in microns.

Figure 14 presents the complete results of the width of bead and depth of dilution measurements across all

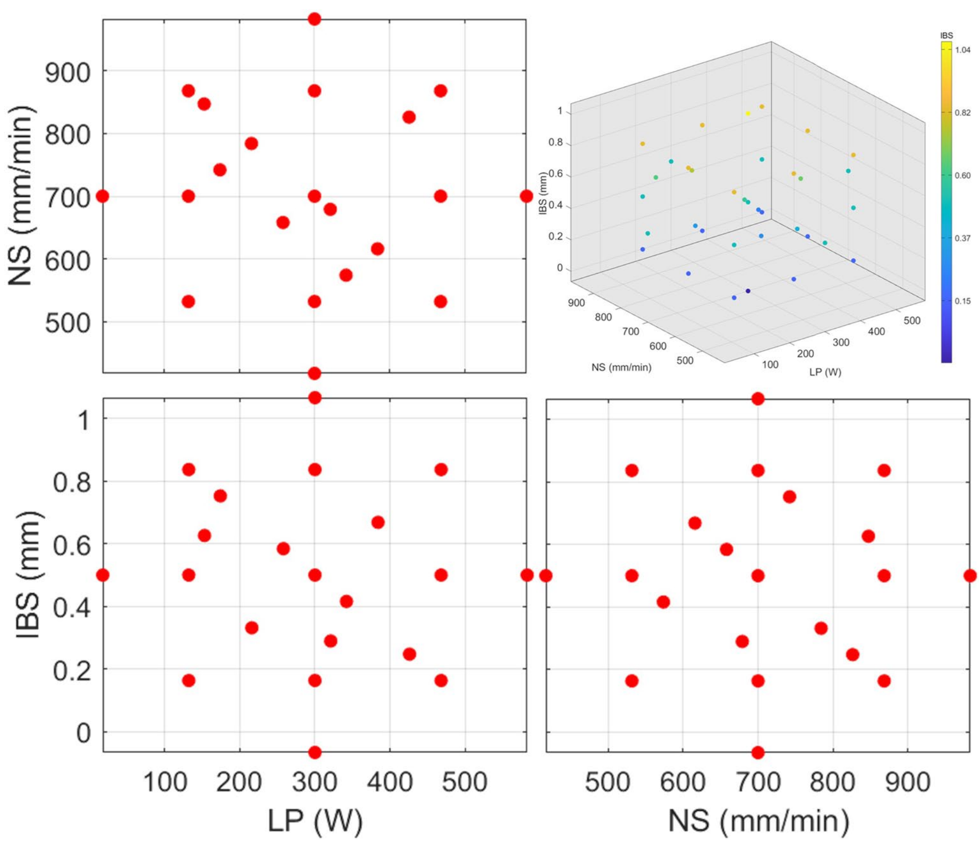

Fig. 12 3D and pairwise projections of the experimental variables based on the combined Space-Filling Design (Sobol Sequence) and Classical Design (Central Composite Design, CCD)

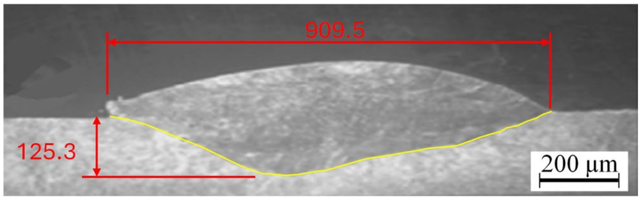

Fig. 13 Cross-section and surface view of bead geometry (No. 20). Powder: Inconel 718; Base metal: STS 316 L. Parameters: Laser power: 300 W; Nozzle speed: 500 mm/min; Powder feed rate: 8 g/min. Fixed Parameters: Coaxial gas: 6 L/min; Feeding gas: 3.5 L/min. OM image captured using Axiolab 5 (Zeiss, Germany). The scale bar is shown in the image

observations, with error bars indicating measurement variability.

Width of bead varied between 450.9 μm and 1279 μm, while depth of dilution ranged from 29.8 μm to 143.1 μm, demonstrating the strong influence of process parameters on bead geometry. The observed variance suggests that different parameter combinations led to distinct bead formations, emphasizing the need for careful process control.

4.1.2 ANN training results

The Artificial Neural Network (ANN) was trained using experimental data, employing the developed systematic grid search approach to evaluate performance and select the best model, as described in Sect. 2.2. The process addressed overfitting and underfitting by determining the optimal number of neurons and layers. Model configurations were assessed using Root Mean Square Error (RMSE) across training (70%), testing (15%), and validation (15%) datasets, ensuring a balance between complexity and generalization.

Table 2 summarizes the training results, showing that the optimized ANN model achieved high correlation

Fig. 14 Results of the width of bead and depth of dilution measurement of the observations

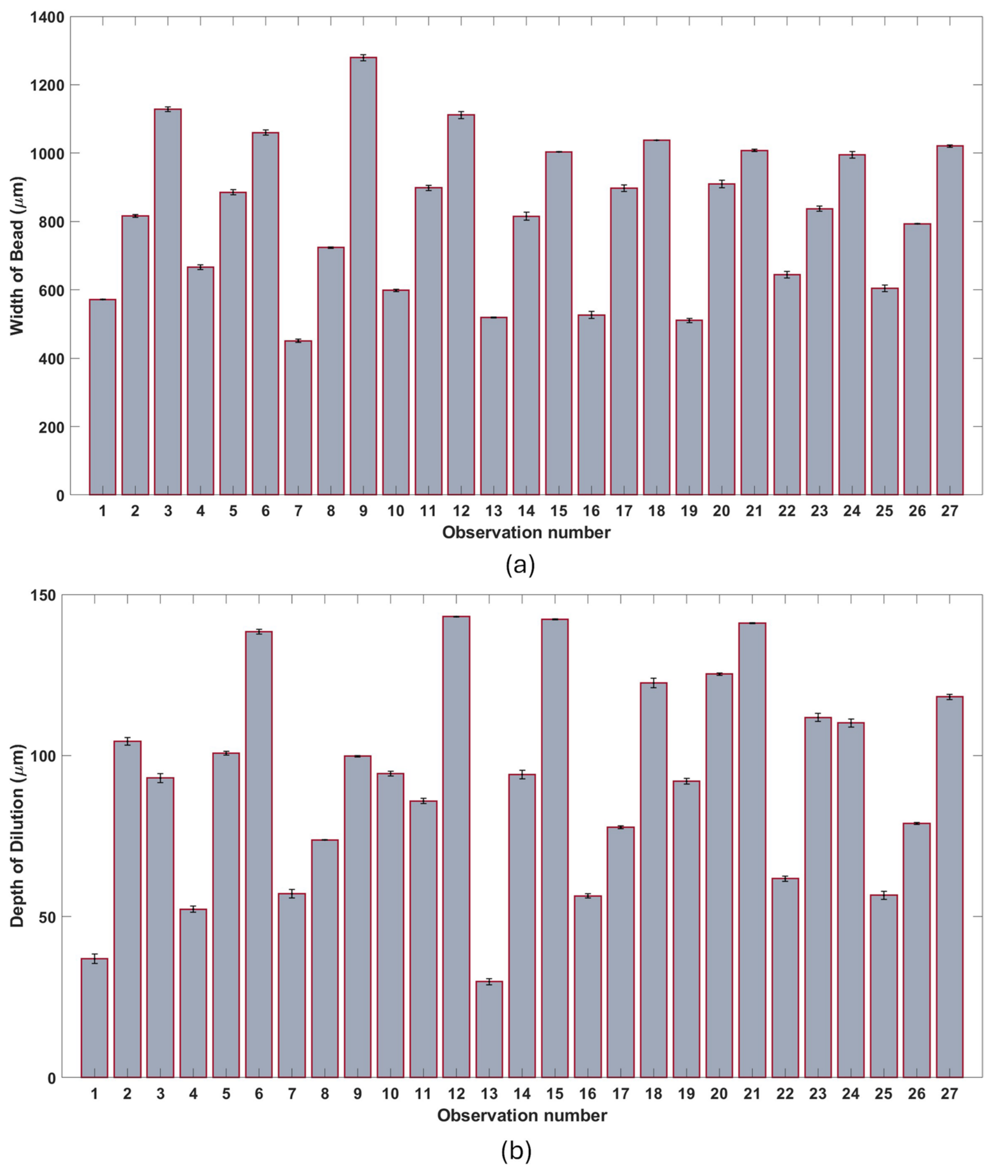

Table 2 Summary of ANN training results for Single-Bead fabrication

Objective	Width of bead	Depth of Dilution
Neurons in the input layer	3	3
Number of hidden layers	1	1
Neurons in the hidden layer	3	3
Neurons in the output layer	1	1
Training algorithm	Levenberg–Marquardt Back-Propagation	Levenberg–Marquardt Back-Propagation
Activation function (Hidden Layer)	Tansig	Tansig
Activation function (Output Layer)	Purelin	Purelin
Validation data fraction (%)	15	15
Test data fraction (%)	15	15
RMSE	47.53	9.05
R_{Train}	0.977	0.974
R_{Test}	0.983	0.970
$R_{Validation}$	0.998	0.958
R_{Total}	0.975	0.958

Table 3 Statistical metrics for ANN prediction error in bead geometry (n=27)

Metric	Width of bead	Depth of Dilution
Sample size (n)	27	27
Mean absolute percentage error (%)	5.03	9.01
Standard deviation (%)	5.69	9.98
95% confidence interval of the mean (%)	±2.23	±3.91
Minimum absolute % error	0.0056	0.2268
Maximum absolute % error	24.4120	45.0288
Median absolute % error	2.39	7.63

coefficients (R_{Total} = 0.975 for width of bead and R_{Total} = 0.958 for depth of dilution) and low RMSE values.

To further quantify the predictive reliability of the trained surrogate models, statistical error metrics were computed for all 27 DOE samples. These metrics include the mean absolute percentage error (MAPE), standard deviation, 95% confidence interval of the mean (CI95), and the distribution limits of the absolute percentage error. Table 3 summarizes these results for bead width and dilution depth.

Figure 15 illustrates the ANN model's predictive performance. Panels (a) and (c) display a strong correlation between predicted and observed values for width of bead and depth of dilution, confirming the model's reliability. Panels (b) and (d) compare ANN predictions with experimental data across different observations, showing that while minor variations exist, the model effectively captures overall trends. These small deviations likely stem from inherent process variability rather than fundamental model limitations. Overall, the ANN demonstrates high predictive accuracy for both width of bead and depth of dilution.

Additional ANN diagnostic plots for the single-bead case, including predicted-versus-measured correlations for the training, validation, and test sets, a test-set residual histogram, and a representative learning-curve figure, are provided in the Supplementary Material.

4.1.3 Sensitivity analysis results

Sensitivity analysis was performed using both the PaD, weights-based, and profile method to determine the influence of each input parameter on width of bead and depth of dilution.

Figure 16 presents the predicted surfaces of two objective functions—width of bead and depth of dilution—versus design parameters: NS (mm/min), PFR (g/min), and LP (W). In the top row (a-c), the width of bead shows a consistent increase with higher NS, PFR, and LP values. Specifically, increasing NS and LP tends to broaden the bead, while PFR has a more subtle influence on the width of bead. The interaction between NS and PFR creates a complex surface, with higher PFR values resulting in larger width of beads, especially at lower processing speeds. The depth increases with higher NS and PFR, particularly at higher power levels (LP), but at lower NS and LP, the increase in depth becomes less significant, suggesting a threshold effect where dilution is less sensitive to parameter changes. These results suggest that increased processing speed, power, and feed rate all contribute to deeper dilution and wider beads. However, at higher power settings, the effect appears to stabilize, indicating a possible saturation point where additional power yields diminishing improvements in dilution depth.

Partial derivative method (PaD) results Figure 17 presents the scatter plots of the partial derivatives of width of bead and depth of dilution with respect to the key process parameters: Laser Power (LP), Nozzle Speed (NS), and Powder Feed Rate (PFR). These plots provide insights into how changes in these input parameters influence the width of bead and dilution depth at a local level, revealing trends and variability in sensitivity.

The first row of scatter plots illustrates the partial derivatives of width of bead with respect to Laser Power (LP), Nozzle Speed (NS), and Powder Feed Rate (PFR). The LP plot (a) reveals a nonlinear relationship, where width of bead remains relatively stable at lower LP values (~200–250 W) but shows increased variability at higher LP values (>300 W). This suggests that higher LP amplifies its influence on width of bead, likely due to increased energy

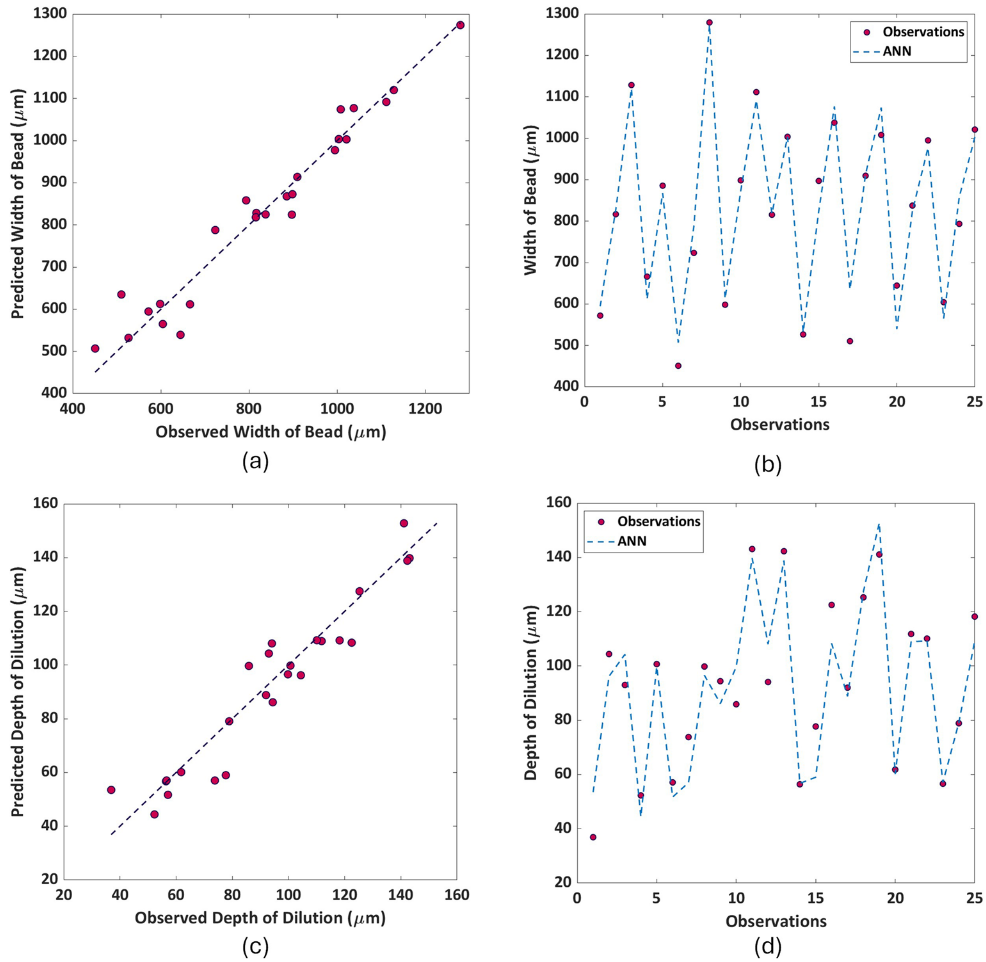

Fig. 15 ANN predictions compared to experimental observations for single-bead objectives: (**a**) Predicted vs. observed width of bead, (**b**) Comparison of width of bead observations and ANN predictions across datasets, (**c**) Predicted vs. observed depth of dilution, (**d**) Comparison of depth of dilution observations and ANN predictions across datasets

input affecting material flow and bead expansion. The NS plot (b) suggests a weak direct effect, as most derivative values cluster around zero, indicating minimal impact under typical operating conditions. However, a subset of points at higher NS values displays more variation, suggesting localized effects, possibly due to secondary interactions like heat accumulation or variations in material deposition rate. The PFR plot (c) shows that increasing PFR generally widens the bead, with most derivative values being positive. However, scattered negative values indicate that in some cases, excessive powder feed may lead to inconsistent bead formation, likely due to unstable material flow. These apparent inconsistencies between the response surface trends (Fig. 16) and the partial derivative plots (Fig. 17) arise from the distinction between global and local sensitivities: response surfaces show average behavior across the design space, while partial derivatives reflect local gradients that may vary significantly in magnitude and direction.

The second row of scatter plots represents the partial derivatives of depth of dilution with respect to LP, NS, and PFR. The LP plot (d) reveals a nonlinear dependency, where depth of dilution remains stable at lower LP but exhibits increased sensitivity at higher power levels. This suggests that higher LP leads to greater dilution effects, likely due to deeper laser penetration affecting dilution depth. The NS plot (e) exhibits a broad spread of values, predominantly negative, indicating that increasing NS reduces depth of dilution. This aligns with expectations, as higher scanning speeds reduce heat input per unit length, leading to shallower penetration and lower dilution depth. However, some points cluster near zero, suggesting minimal effects in certain operational conditions. The PFR plot (f) shows a mixed distribution of positive and negative values, suggesting a more complex relationship between PFR and dilution depth. While higher PFR generally increases dilution variability, the scattered distribution indicates an interplay between mass flow rate and heat input, affecting dilution differently under varying conditions.

Figure 17 confirms that LP is the dominant factor influencing width of bead, with its effect becoming more pronounced at higher power levels. For depth of dilution, NS remains the most significant controlling factor, exhibiting a strong negative correlation as scanning speed increases. PFR contributes to width of bead formation, with higher

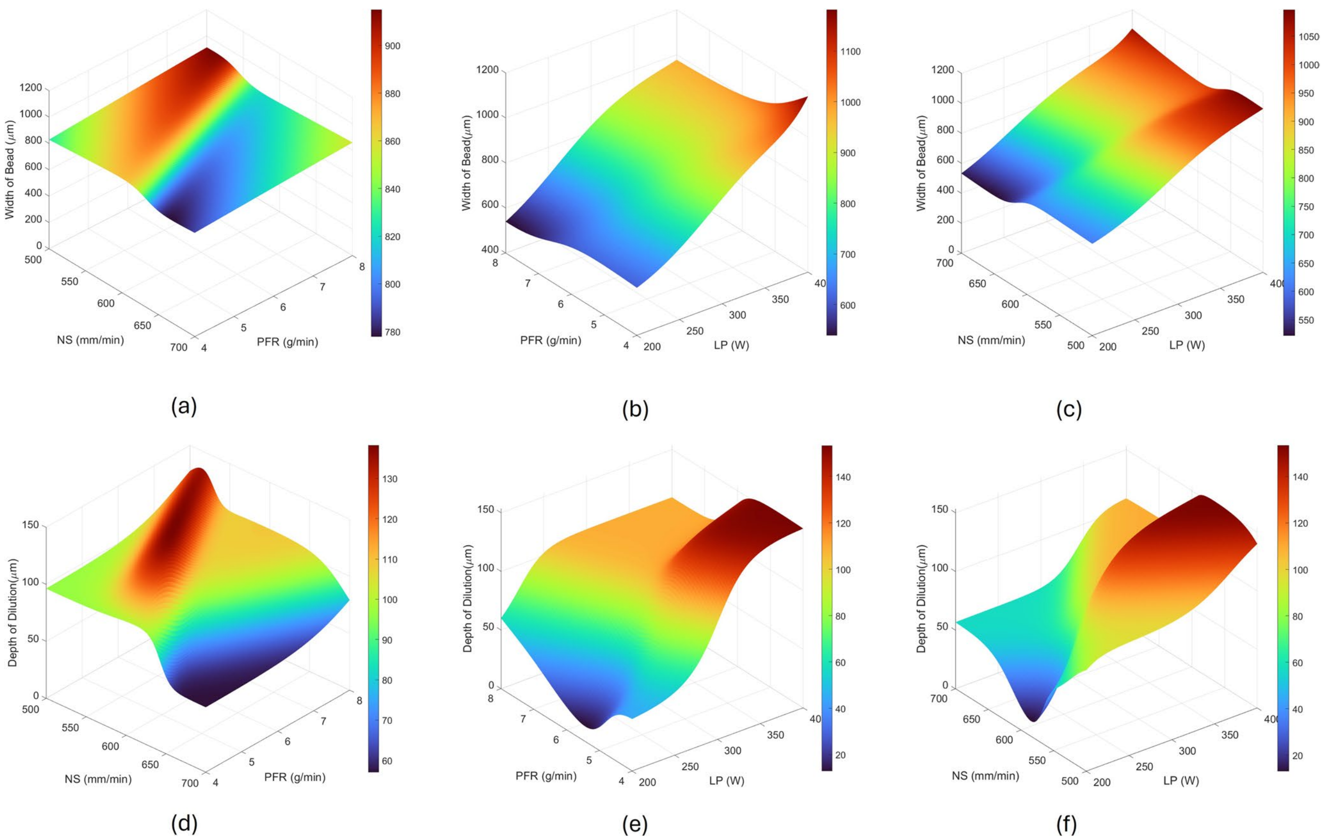

Fig. 16 ANN-predicted response surfaces for single-bead objectives as functions of key process parameters. (**a-c**) Width of bead variations with NS (mm/min), PFR (g/min), and LP (W). (**d-f**) Depth of dilution variations with NS (mm/min), PFR (g/min), and LP (W)

values generally leading to wider beads. However, its effect on dilution is more variable, likely due to complex interactions between powder flow, heat input, and material penetration.

The total contribution of each parameter to width of bead and depth of dilution was calculated using Eq. (8). For width of bead, LP contributes 88.42%, NS accounts for 8.45%, and PFR has a minor effect at 3.13%. For depth of dilution, LP contributes 42.28%, NS is the dominant factor at 45.10%, and PFR accounts for 12.63%.

These results further confirm that LP remains the dominant influencing factor for both width of bead and depth of dilution, though its effect is highly variable. NS has a moderate effect on dilution but plays a secondary role in bead width, while PFR has the least contribution overall. This reinforces the need for careful LP and NS adjustments to optimize process performance.

Bootstrap-based robustness verification and kernel density–based diagnostic distributions of the PaD sensitivities, used to assess variability and ranking stability, are provided in the Supplementary Material.

Weights-Based sensitivity results For width of bead, the weights-based sensitivity analysis (calculated using Eq. (11) for Relative Importance (RI)) reveals that Laser Power (LP) contributes the most (53.43%), followed by Nozzle Speed (NS) (27.99%) and Powder Feed Rate (PFR) (18.57%). This suggests that LP plays the most dominant role in bead width formation, likely due to its direct influence on energy input and material flow dynamics. NS has a moderate effect, which may be attributed to its impact on deposition uniformity and bead spreading behavior, while PFR has the least influence, indicating that variations in powder flow affect bead width to a lesser extent compared to LP and NS.

For depth of dilution, NS is identified as the most influential parameter (46.73%), followed by LP (28.71%) and PFR (24.54%). The strong influence of NS suggests that it is the primary factor controlling dilution depth, likely due to its direct effect on heat input per unit length, which governs penetration depth. LP remains an important factor, as higher power levels enhance material melting and fusion depth. PFR contributes less significantly, suggesting that variations in powder flow have a moderate but non-dominant effect on dilution.

Figure 18a and b present heatmaps of the absolute weight magnitudes, visually confirming these findings. The brighter intensity for LP in Fig. 19a (width of bead) reinforces its

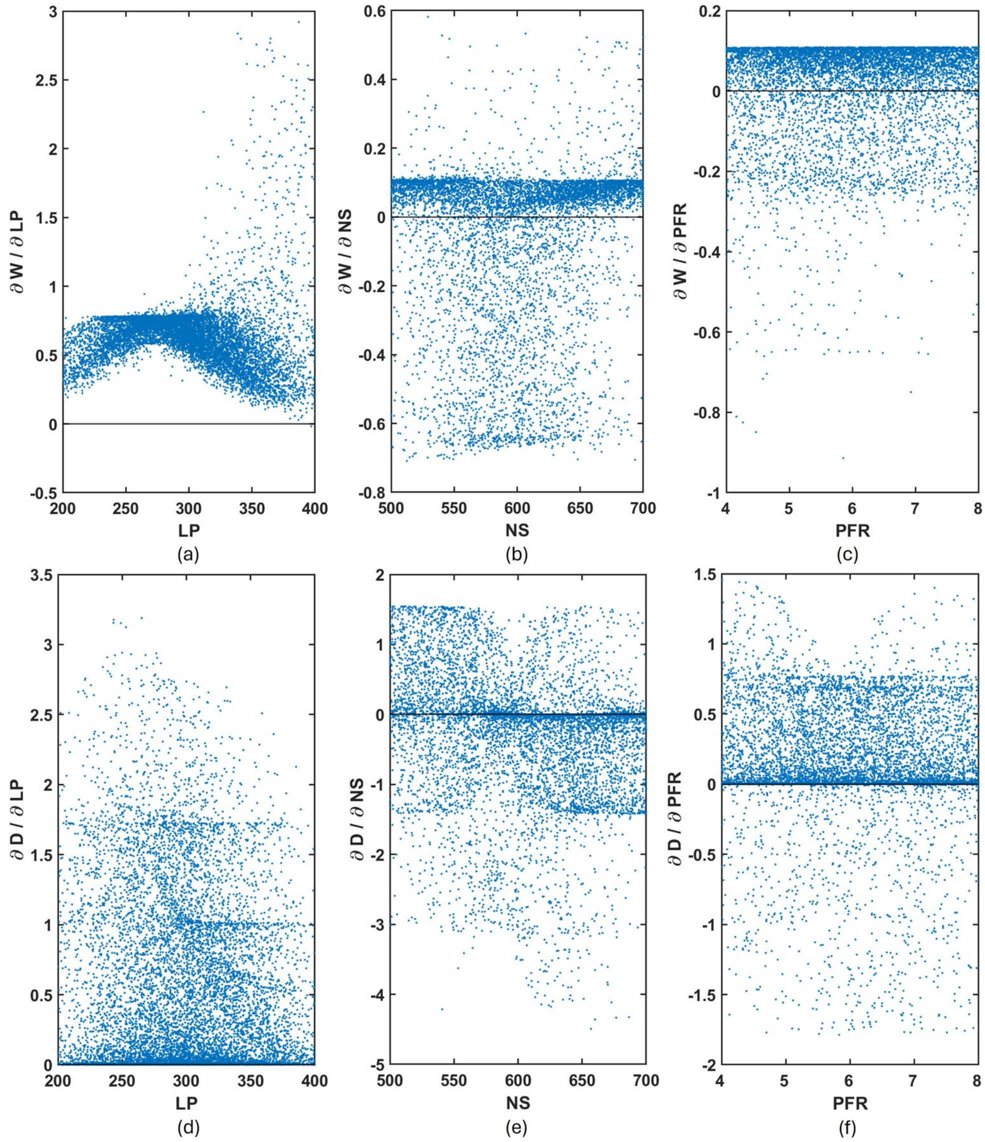

Fig. 17 Partial derivative analysis illustrating the sensitivity of width of bead (**a**–**c**) and depth of dilution (**d**–**f**) with respect to Laser Power (LP), Nozzle Speed (NS), and Powder Feed Rate (PFR). The scatter plots show how each process parameter influences bead geometry and dilution depth, highlighting LP as the dominant factor

dominant influence, whereas NS exhibits stronger weight connections in Fig. 19b (depth of dilution), aligning with its higher importance in controlling dilution depth. The relative contrast of weights across neurons further illustrates the underlying nonlinear relationships between process parameters and output responses.

Profile method results Figure 19 presents the contribution profiles of Laser Power (LP), Nozzle Speed (NS), and Powder Feed Rate (PFR) in determining width of bead (left) and depth of dilution (right) using the Profile Method at the highest resolution scale (192 variation intervals). The influence of each input variable was assessed across multiple scales (12, 24, 48, 96, 144, and 192) to ensure stable contribution estimates and confirm the consistency of sensitivity rankings.

For width of bead, LP exhibits a strong increasing trend (~72.7% in the Profile Method), reinforcing its primary role in bead expansion. The PaD method assigns an even higher influence to LP (~88.42%), while the weights-based method provides a more balanced sensitivity ranking, with LP (53.43%) and NS (27.99%). NS plays a moderate role (~16.4% in the Profile Method), likely contributing to deposition uniformity and material spreading. PFR remains the least influential (~10.9%), though its effects are more localized. Across different sensitivity methods, the rankings remain stable, confirming the robustness of the analysis.

For depth of dilution, NS emerges as the most significant factor (~50.05%), initially exhibiting a strong increasing influence before stabilizing at higher scanning speeds. This

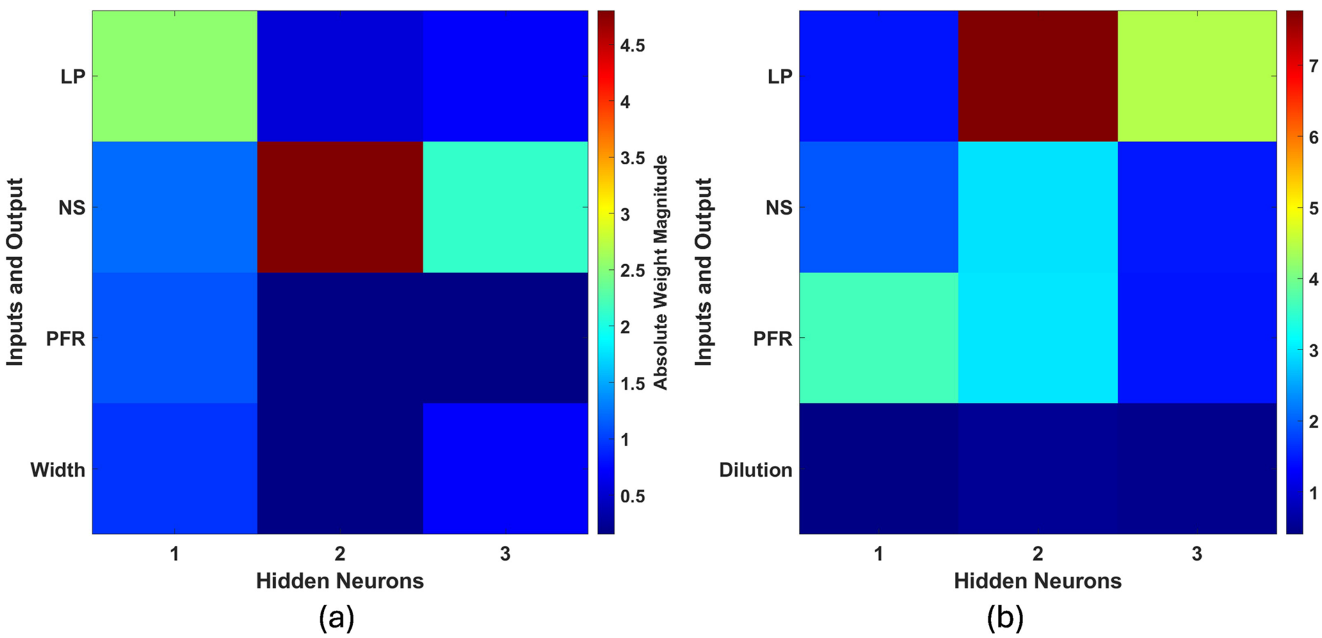

Fig. 18 (**a**) Heatmap of absolute weight magnitudes for Width of Bead, illustrating the dominant influence of Laser Power (LP). (**b**) Heatmap of absolute weight magnitudes for Depth of Dilution, highlighting Nozzle Speed (NS) as the most significant parameter

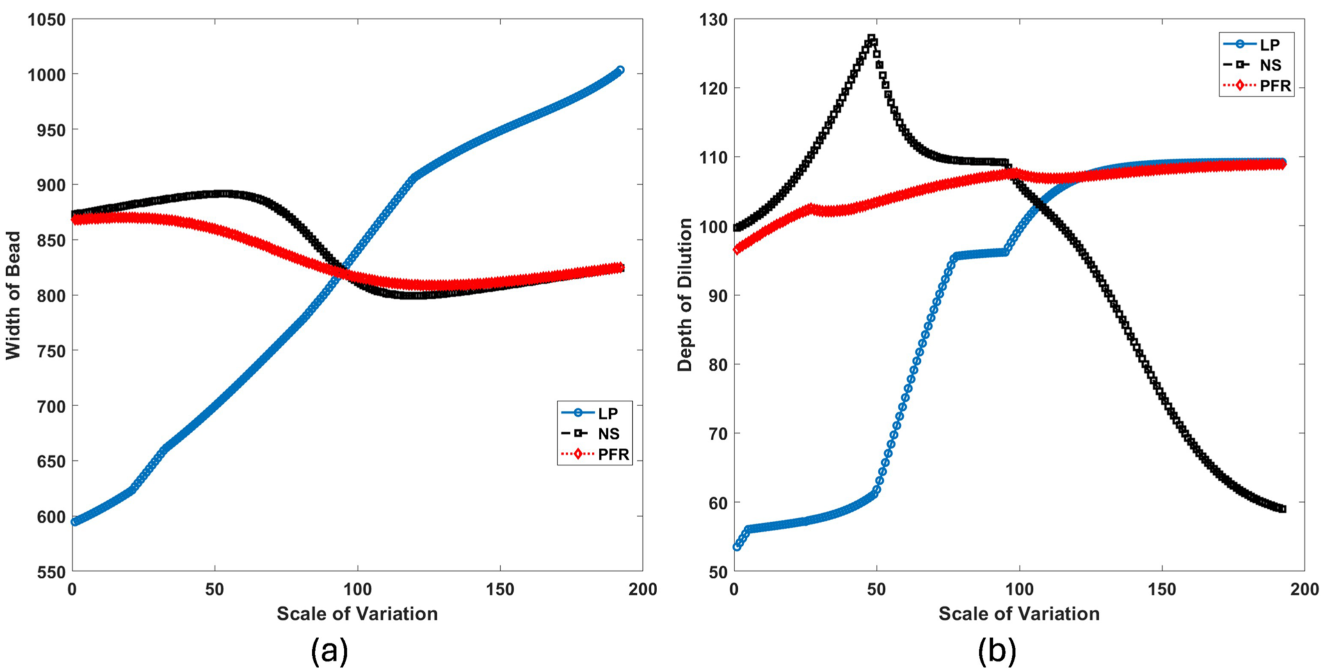

Fig. 19 Influence of Laser Power (LP), Nozzle Speed (NS), and Powder Feed Rate (PFR) on (**a**) Width of Bead and (**b**) Depth of Dilution using the Profile Method at 192 variation intervals. The analysis was conducted across multiple scales (12, 24, 48, 96, 144, and 192) to ensure convergence

suggests that while NS initially governs penetration depth by controlling heat input per unit length, its effect diminishes as processing speed exceeds a certain threshold. LP (~40.88%) also plays a substantial role, with a nonlinear response indicating that higher power levels enhance dilution depth up to a saturation point. In contrast, PFR (~9.07%) shows a relatively stable but minor contribution, reinforcing that powder flow rate affects dilution depth less directly. As the scale resolution increases, the rankings remain consistent, confirming the robustness of the analysis.

Comparative analysis of sensitivity methods To comprehensively evaluate the influence of process parameters, three different sensitivity analysis methods were applied:

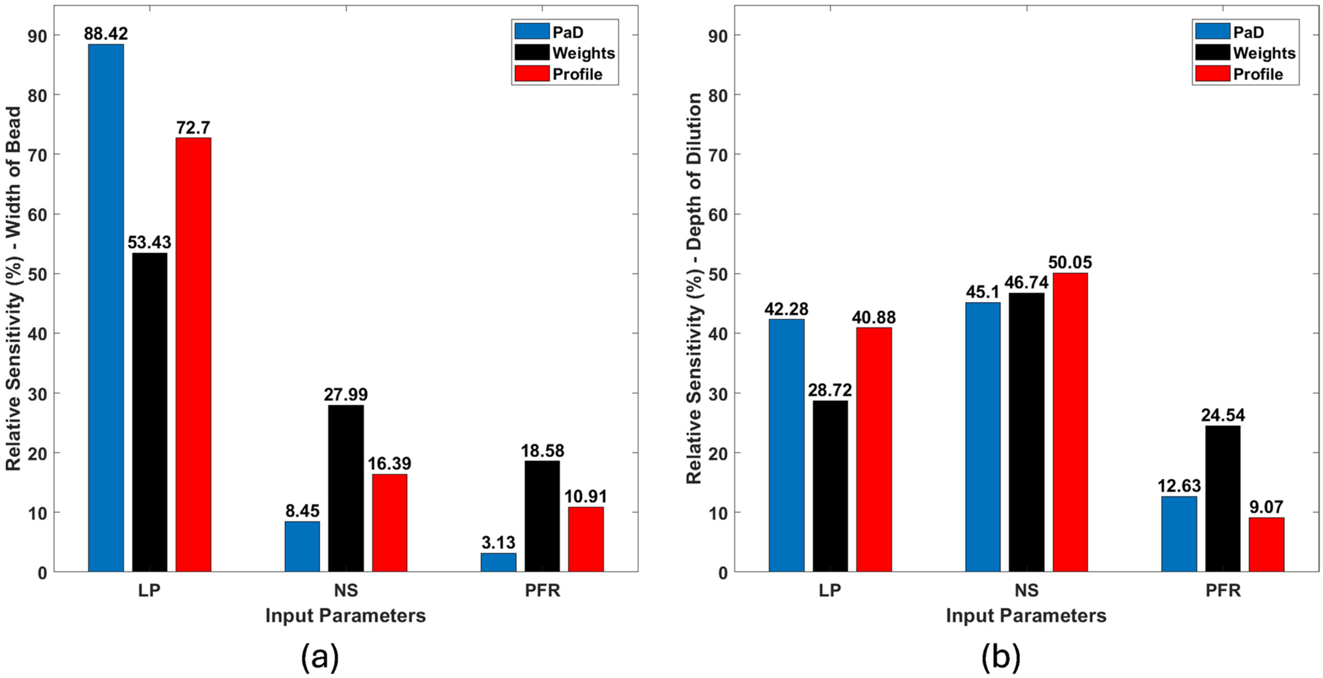

Fig. 20 (**a**) Sensitivity analysis results for Width of Bead using the PaD, Weights-Based, and Profile Method, confirming LP as the dominant parameter across all approaches. (**b**) Sensitivity analysis results for Depth of Dilution, where NS is consistently identified as the most influential factor

Table 4 Summary of sensitivity contributions and rankings across methods

Parameter	PaD Method (%)	Weights Method (%)	Profile Method (%)	Average Rank
Width of Bead				
LP	**88.42**	**53.43**	**72.7**	**1**
NS	8.45	27.99	16.39	2
PFR	3.13	18.58	10.91	3
Depth of Dilution				
LP	42.28	28.72	40.88	2
NS	**45.10**	**46.74**	**50.05**	**1**
PFR	12.63	24.54	9.07	3

the Partial Derivative (PaD) method, the weights-based method, and the Profile Method. The comparative results for Width of Bead and Depth of Dilution are summarized in Fig. 20; Table 4.

Width of Bead Sensitivity The PaD method assigns the highest sensitivity to Laser Power (LP) (88.42%), followed by Nozzle Speed (NS) (8.45%) and Powder Feed Rate (PFR) (3.13%). The weights-based method also ranks LP as the most significant factor (53.43%), but assigns higher importance to NS (27.99%) and PFR (18.58%) compared to PaD. The Profile Method, which systematically varies input parameters while holding others constant, confirms LP as the most dominant factor (72.7%), followed by NS (16.39%) and PFR (10.91%).

While all three methods consistently rank LP as the primary influencing factor, the relative importance of NS and PFR varies. The PaD method, which captures local sensitivities based on network gradients, emphasizes LP more strongly. In contrast, the weights-based and profile methods, which account for global interactions, show a higher contribution of NS and PFR.

Depth of Dilution Sensitivity For depth of dilution, NS is consistently identified as the most significant parameter across all three methods. The Profile Method assigns 50.05% influence to NS, followed by LP (40.88%) and PFR (9.07%). Similarly, the weights-based method ranks NS (46.74%) as the dominant factor, with LP (28.72%) and PFR (24.54%) contributing to a lesser extent. The PaD method suggests a more balanced influence between NS (45.10%) and LP (42.28%), while PFR remains minor (12.63%).

Although all three methods confirm NS as the dominant factor for depth of dilution, the PaD method assigns a more comparable influence to LP, reflecting differences in how these techniques assess sensitivity. PaD captures localized variations in input-output gradients, which may exaggerate the importance of certain parameters in specific regions. In contrast, the weights-based and profile methods provide a more holistic evaluation, capturing broader trends in process behavior. By integrating all three approaches, a more comprehensive understanding of process sensitivity is achieved, ensuring reliable parameter tuning for optimal DED performance.

Summary of Sensitivity Rankings Despite some numerical differences, the rankings remain consistent across methods, as shown in Table 4, reinforcing the reliability of the sensitivity analysis.

Rank-Correlation Analysis Across Sensitivity Methods To quantify the level of agreement among sensitivity methods, Spearman's ρ and Kendall's τ were computed for all pairwise comparisons. Because the three techniques produced identical rankings for both Width of Bead (LP → NS → PFR) and Depth of Dilution (NS → LP → PFR), the rank-correlation metrics indicate perfect consistency, with Spearman's ρ = 1.000 and Kendall's τ = 1.000 across all method pairs.

The complete rank-correlation matrix is provided in Table 5, confirming that the parameter hierarchy is entirely stable and independent of the chosen sensitivity method.

This full agreement demonstrates that the ANN-based framework captures stable internal relationships between input parameters and outputs. LP governs bead width, while NS is the principal factor controlling dilution depth.

Interpretation and Physical Consistency The physical meaning of these trends is consistent with established melt-pool behavior, as summarized below:

- **Laser Power (LP)** governs the total energy input, explaining its dominant role in bead width formation.
- **Nozzle Speed (NS)** controls the energy density delivered per unit length, making it the primary determinant of dilution depth.
- **Powder Feed Rate (PFR)** influences mass addition but has a comparatively weaker effect on melt-pool energetics, resulting in consistently low sensitivity across all methods.

Table 5 Rank-Correlation summary for Single-Bead sensitivity analysis

Objective	Methods Compared	Spearman ρ	Kendall τ	Rank Ordering
Width of Bead	PaD vs. Weights	1.000	1.000	LP > NS > PFR
	PaD vs. Profile	1.000	1.000	LP > NS > PFR
	Weights vs. Profile	1.000	1.000	LP > NS > PFR
Depth of Dilution	PaD vs. Weights	1.000	1.000	NS > LP > PFR
	PaD vs. Profile	1.000	1.000	NS > LP > PFR
	Weights vs. Profile	1.000	1.000	NS > LP > PFR

Because PaD, weights-based, and profile analyses produce identical rankings, the resulting sensitivity hierarchy is both computationally robust and physically meaningful, reinforcing confidence in the reliability of the ANN-based single-bead analysis.

4.1.4 Multi-objective optimization

The NSGA-II optimization generated a Pareto front that captures the trade-off between width of bead and depth of dilution. A complete view of the optimization behaviour is presented through the convergence history (Fig. 21a), the stability analysis across multiple runs (Fig. 21b), and the final Pareto front with the selected solution (Fig. 21c). Each point on the Pareto front represents a non-dominated solution, where improving one objective necessarily compromises the other. The final selection therefore depends on process priorities, ensuring an optimized balance between bead geometry and dilution depth.

Explicit objective normalization was not applied in the NSGA-II optimization because both objectives in the single-bead case—width of bead and depth of dilution—are expressed in the same physical unit (µm) and exhibit comparable numerical magnitudes over the explored design space. Under such well-conditioned two-objective settings, Pareto dominance relationships are invariant to linear scaling, and MATLAB's *gamultiobj* solver can operate directly on the raw objective values without introducing scale bias. This approach avoids artificial weighting effects and preserves the physical interpretation of the trade-off between bead geometry and dilution behavior.

To ensure robust convergence and adequate exploration of the design space, MATLAB's *gamultiobj* solver was configured using the parameters summarized in Table 6. These settings follow standard NSGA-II guidelines for low-dimensional, nonlinear multi-objective problems.

NSGA-II convergence was evaluated using the Pareto spread, which measures the distribution of solutions across the front. Figure 21a shows rapid spread reduction within the first ~ 30 generations, followed by a smooth stabilizing trend, confirming consistent convergence toward a well-defined trade-off curve. Complementary diversity plots further verify that the solver maintains adequate population diversity throughout the optimization.

To further verify robustness and exclude sensitivity to random initialization, NSGA-II was executed five independent times using different random seeds. The resulting Pareto fronts, shown in Fig. 21b, overlap closely despite the stochastic nature of evolutionary algorithms. This indicates

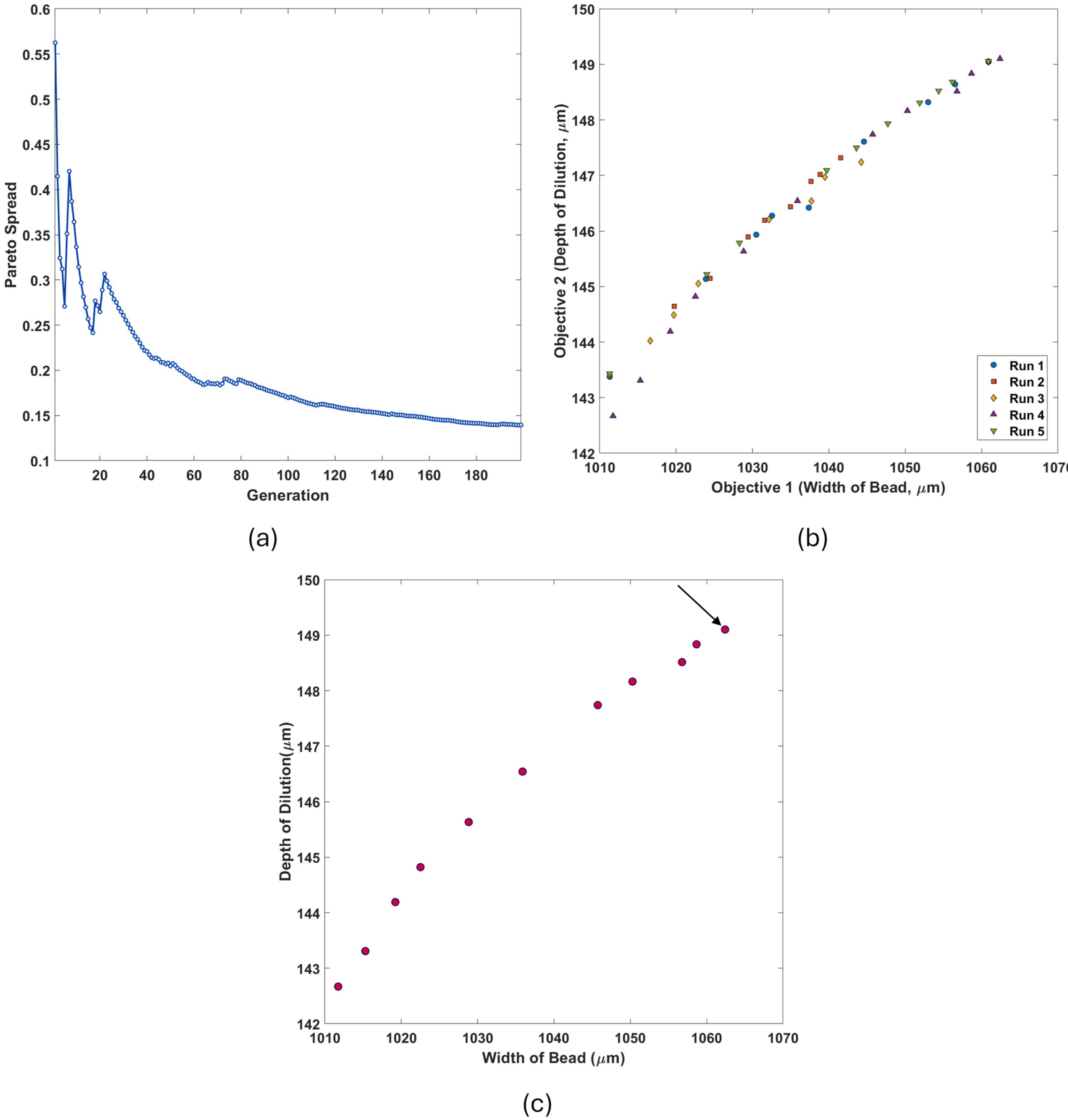

Fig. 21 (**a**) NSGA-II convergence curve. (**b**) Stability of NSGA-II Pareto fronts across five independent solver runs. The overlapping fronts confirm strong robustness and repeatability of the optimization process. (**c**) Final Pareto front and selected solution for single bead fabrication

high run-to-run repeatability, strong numerical stability, and confirming that the reported Pareto front is not an artifact of a particular solver state.

The final selected solution prioritizes maximum depth of dilution while maintaining an acceptable bead width close to 1000 µm, as defined in Eq. (13). As expected, reducing bead width typically lowers dilution depth, reinforcing the inherent trade-off between the two objectives. The ANN–NSGA-II framework effectively captured and balanced these competing responses.

The overall optimization results are summarized in Table 7, including the predicted and experimental objectives and the corresponding prediction errors.

This comprehensive optimization process demonstrates the robustness of the ANN-NSGA-II framework in balancing conflicting objectives while ensuring high prediction

Table 6 NSGA-II configuration used in single bead optimization

Parameter	Value
Population size	50
Pareto fraction	0.20
Crossover fraction	0.80
Crossover function	Intermediate (ratio = 1.0)
Mutation	Adaptive (default)
Migration	Forward, 0.20 fraction
Maximum generations	200
Stall generations	100
Function tolerance	1×10^{-4}
Constraint tolerance	1×10^{-3}
Stopping criterion	Average change in Pareto spread below tolerance
Number of independent runs	5 (for stability analysis)

Table 7 Overall optimization summary for single bead fabrication

Parameter/Objective	Value
Laser Power (W)	374.595 (374)
Feed Rate or Nozzle Speed (mm/min)	570.937 (570.94)
Powder Feed Rate (g/min)	4.6977 (4.7)
Predicted Width of Bead (µm)	1062.408
Experimental Width of Bead (µm)	1018.7
Width of Bead prediction error (%)	4.11
Predicted Depth of Dilution (µm)	149.101
Experimental Depth of Dilution (µm)	147.2
Depth of Dilution prediction error (%)	1.28

accuracy. The low prediction errors, 4.11% for width of bead and 1.28% for depth of dilution, confirm the reliability of the framework for guiding additive manufacturing design decisions.

4.2 Case study 2: cube fabrication

This case study focuses on optimizing two key objectives: height of cube and material hardness. Achieving the correct height is critical for ensuring dimensional accuracy, while maintaining sufficient hardness is essential for mechanical performance and part durability.

4.2.1 Experimental results

To explore the influence of process parameters on cube height and hardness, experiments were designed using a combination of Space-Filling Design (Sobol Sequence) and Classical Design (Central Composite Design, CCD). This hybrid approach leverages the strengths of both methodologies—Sobol Sequence ensures a well-distributed exploration of the design space, while CCD enables precise modeling of nonlinear interactions.

The key input parameters considered in this study were laser power (LP), feed rate (FR), and inter-bead spacing (IBS). Fabricated cubes were analyzed across 35 trials, with their height and hardness measured to evaluate the impact of process variations. Figure 22 presents images of the fabricated cubes and an example of the height measurement procedure.

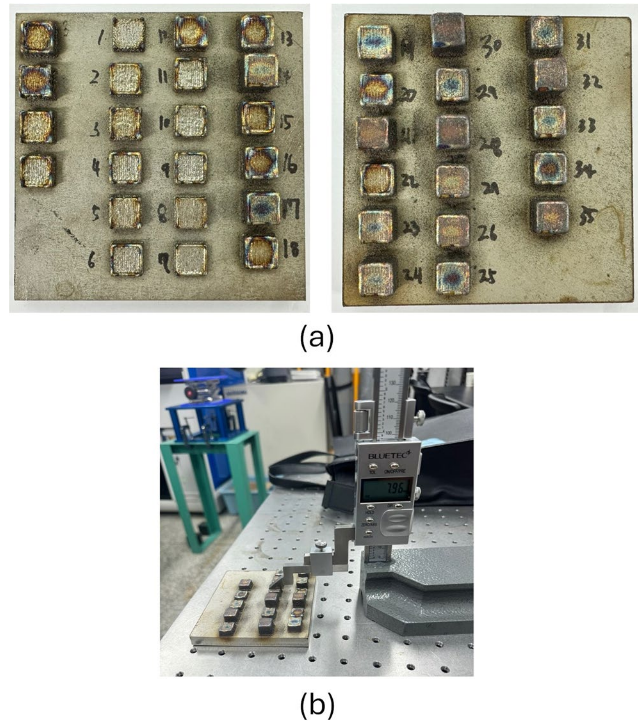

Fig. 22 Additive-manufactured cubes and height measurement. Powder: Inconel 718; Base metal: STS 316 L. Fixed Parameters: Coaxial gas (Argon): 4 L/min; Feeding gas (Argon): 7 L/min; Powder feed rate: 4.7 g/min; Z-pitch: 0.25 mm

For each fabricated cube, height and hardness were measured with repeated readings to account for normal instrument variability. Cube height was recorded three times using a digital height gauge by lightly repositioning the probe on the top surface. Micro-Vickers hardness was obtained from multiple indentation readings performed on the polished cross-section prepared after cutting each cube, and the mean value was used for analysis.

Figure 23 illustrates the measured height of cube and hardness across the 35 trials, with error bars indicating measurement variability. The cube height ranged from 1.49 mm to 11.87 mm, while hardness values varied between 219.31 HV and 238.51 HV. The observed variations indicate that inter-bead spacing (IBS) and laser power (LP) played dominant roles, affecting both height uniformity and material hardness distribution. These results highlight the complex interplay between process parameters in additive manufacturing, emphasizing the need for multi-objective optimization strategies.

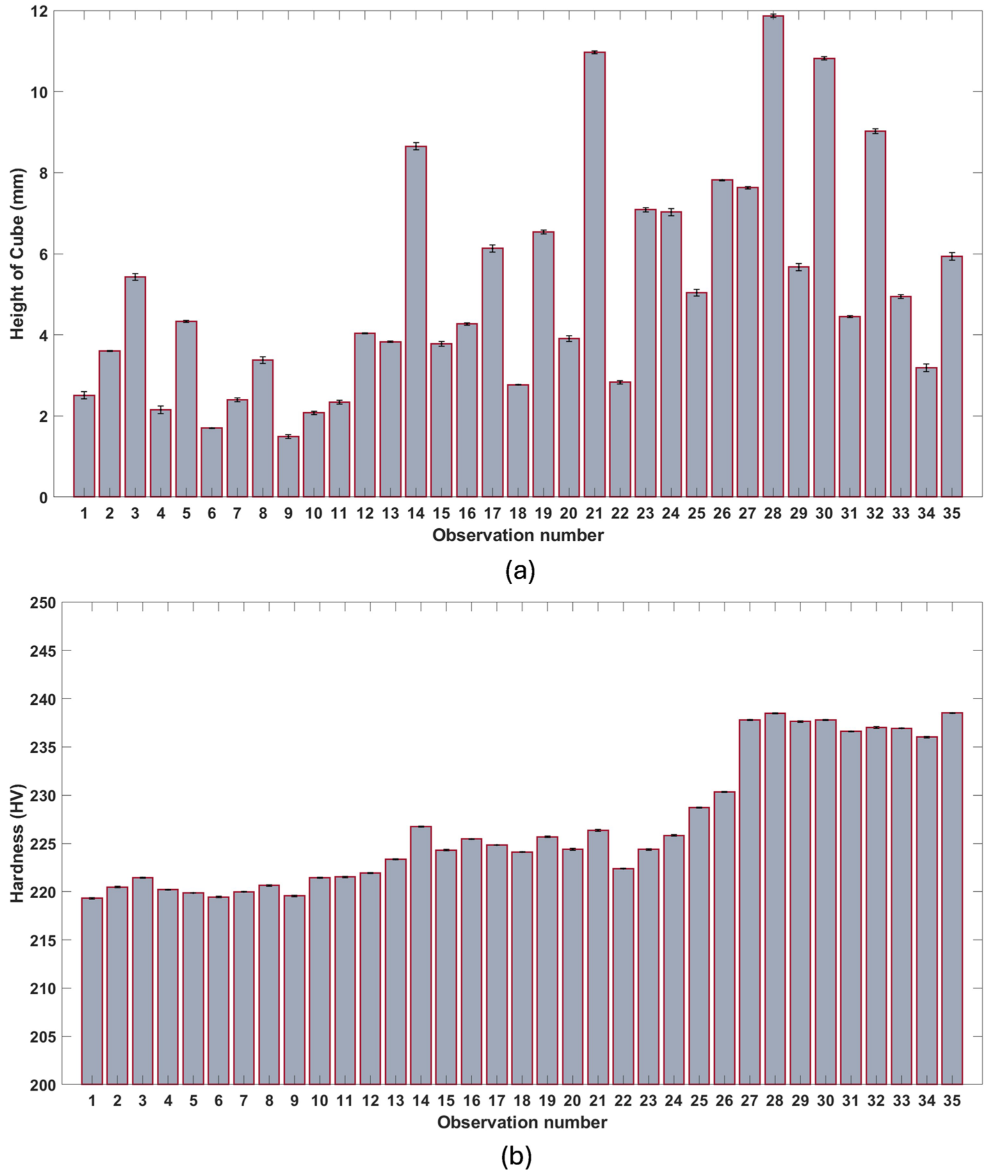

Fig. 23 Results of the height of cube and hardness measurement across 35 trials

4.2.2 ANN training results

The ANN model was trained using experimental data, applying the structured grid search methodology to optimize performance and determine the most effective architecture, as outlined in Sect. 2.2. The model was designed to predict height of cube and hardness, key factors in ensuring both dimensional accuracy and mechanical integrity.

Table 8 summarizes the ANN training results, demonstrating high predictive accuracy. The optimized ANN model achieved high correlation coefficients ($R_{Total} = 0.996$ for Height of Cube and $R_{Total} = 0.997$ for Hardness) along with low RMSE values, confirming its robustness in capturing the relationship between input parameters and target objectives.

To assess the predictive reliability of the surrogate models beyond training statistics, additional error analysis was performed using all 35 DOE samples. Absolute percentage errors were calculated for each experimental–prediction pair, and statistical metrics—including mean error, standard deviation, 95% confidence interval (CI95), and minimum/median/maximum error—were computed. These results are summarized in Table 9 for both height and hardness.

Figure 24 illustrates the ANN's predictive performance for both the height of cube and hardness. Panels (a) and (c) demonstrate a strong correlation between predicted and observed values, confirming the model's reliability. In Panel (b), while the ANN effectively captures overall trends in height prediction, minor discrepancies are observed in some instances. Similarly, in Panel (d), the model accurately follows hardness trends but exhibits greater sensitivity to

Table 8 Summary of ANN training results for cube fabrication

Objective	Height of Cube	Hardness
Neurons in the input layer	3	3
Number of hidden layers	1	1
Neurons in the hidden layer	3	3
Neurons in the output layer	1	1
Training algorithm	Levenberg–Marquardt Back-Propagation	Levenberg–Marquardt Back-Propagation
Activation function (Hidden Layer)	Tansig	Tansig
Activation function (Output Layer)	Purelin	Purelin
Validation data fraction (%)	15	15
Test data fraction (%)	15	15
RMSE	0.245	0.535
R_{Train}	0.996	0.999
R_{Test}	0.997	0.999
$R_{Validation}$	0.999	0.997
R_{Total}	0.996	0.997

Table 9 Statistical metrics for ANN prediction error in cube properties ($n=35$)

Metric	Height of Cube	Hardness
Sample size (n)	35	35
Mean absolute percentage error (%)	5.18	0.152
Standard deviation (%)	4.73	0.185
95% confidence interval of the mean (%)	±1.57	±0.061
Minimum absolute % error	0.080	2.10×10^{-6}
Maximum absolute % error	18.114	0.770
Median absolute % error	3.63	0.099

parameter variations, reflecting the complexity of hardness-related interactions. These results reinforce the ANN's capability to predict both dimensional accuracy and mechanical response, providing a powerful tool for process optimization.

For completeness, additional ANN diagnostic plots for the cube case—including predicted-versus-measured correlations, test-set residual distributions, and a representative learning-curve figure—are provided in the Supplementary Material.

4.2.3 Sensitivity analysis results

Figure 25 presents the predicted surfaces of two objective functions—height of cube and hardness—relative to the design parameters: NS (mm/min), IBS (mm), and LP (W). The height of cube generally decreases with increasing NS and IBS, particularly at higher scanning speeds and larger inter-bead spacing. However, variations occur at higher LP values, indicating nonlinear interactions between power and other process parameters. For hardness, a distinct trend emerges where increased NS, IBS, and LP lead to higher hardness values, especially at elevated power levels. These findings suggest that while higher processing speeds and power enhance material hardness, the combined effects of tool size and power levels introduce more complex influences on height formation.

Partial derivative method (PaD) results Figure 26 presents scatter plots of the partial derivatives of height of cube (H1) and hardness (H2) with respect to Laser Power (LP), Nozzle Speed (NS), and Inter-Bead Spacing (IBS). These plots highlight the local sensitivity of each response variable to changes in the input parameters.

For height of cube (H1) (first row), panel (a) shows a nonlinear sensitivity trend with respect to LP. At lower LP values, the majority of partial derivative values are positive, indicating that increasing laser power enhances height formation due to improved material deposition. However, as LP increases further, derivative values shift toward negative, suggesting that excessive power may alter material flow dynamics or surface energy balance, reducing final height. This highlights the importance of selecting an optimal LP range for controlled vertical growth.

Panel (b) indicates a predominantly negative relationship between Nozzle Speed (NS) and height of cube (H1). As NS increases, the majority of derivative values remain negative, suggesting that higher scanning speeds reduce heat input per unit length, limiting material accumulation and vertical buildup. The spread of values implies process variability, but the overall trend confirms that excessive scanning speed can reduce layer formation by decreasing deposition efficiency.

Panel (c) reveals a positive correlation between Inter-Bead Spacing (IBS) and height of cube (H1). At lower IBS values, mixed derivative trends are observed, but as IBS increases, the derivatives predominantly become positive. This suggests that a moderate IBS facilitates better layer buildup by reducing excessive overlap. However, at very high IBS values, inconsistent derivative behavior is observed, indicating potential instability in fusion efficiency, which may negatively impact height formation.

Panel (d) highlights a nonlinear dependency of Hardness (H2) on Laser Power (LP). At lower LP values, the derivative values remain close to zero or slightly positive, suggesting a weaker influence on hardness. However, as LP increases, a strong positive trend emerges, indicating that higher laser power enhances hardness, likely due to improved material fusion and densification. Some scattered negative derivatives suggest localized effects, possibly

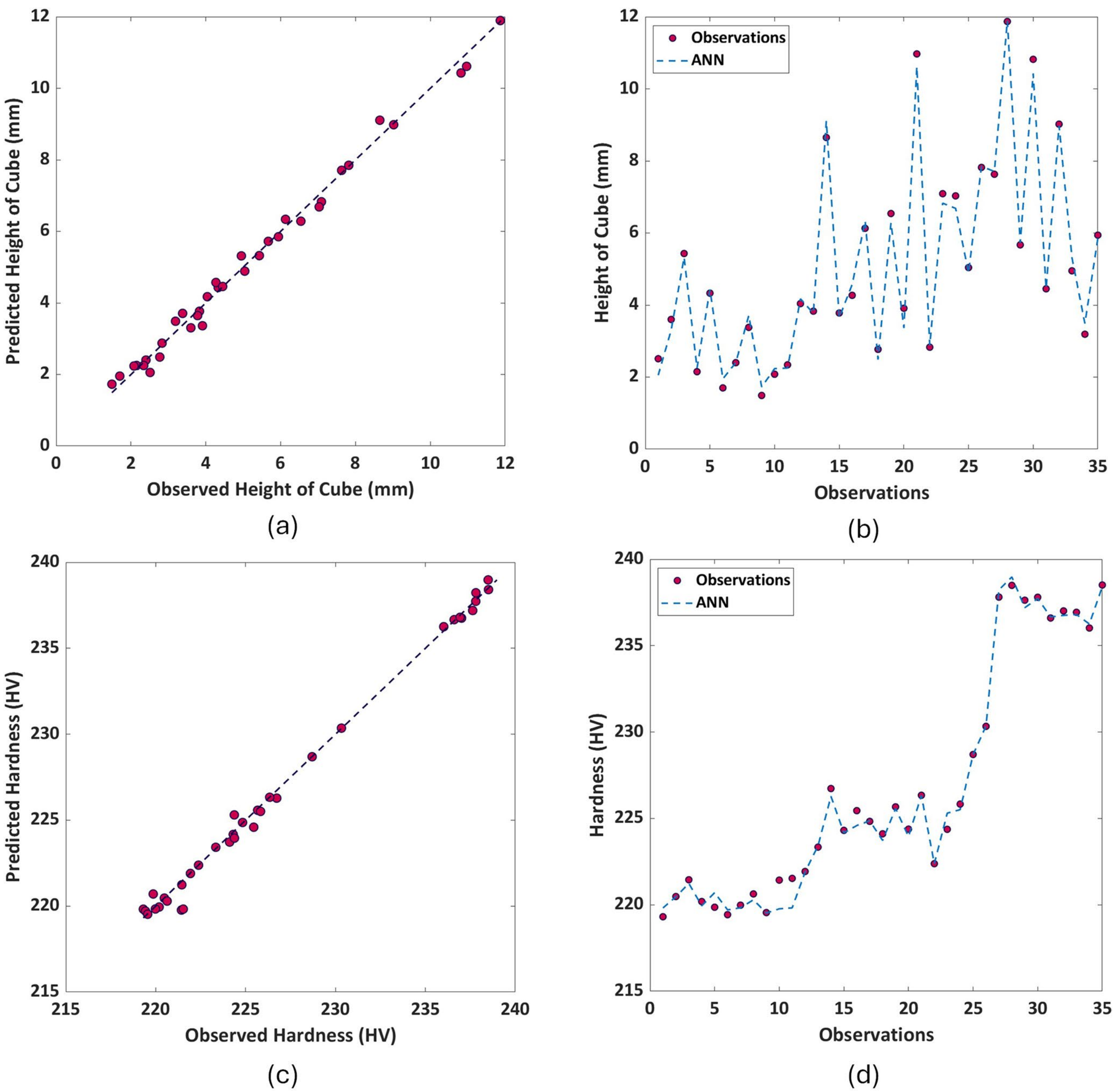

Fig. 24 ANN predictions versus experimental observations for Cube objectives: (**a**) Predicted versus observed Height of Cube, (**b**) Comparison of Height of Cube observations and ANN predictions across datasets, (**c**) Predicted versus observed Hardness, (**d**) Comparison of Hardness observations and ANN predictions across datasets

due to grain coarsening or thermal softening in overheated regions.

Panel (e) suggests a primarily negative correlation between Nozzle Speed (NS) and hardness (H2). As NS increases, hardness tends to decrease, likely due to reduced heat input per unit area, which limits material densification. However, at very high NS, competing effects such as refined grain structures due to altered cooling rates may also occur. The trend is more stable compared to height sensitivity, indicating that NS consistently affects hardness by controlling fusion efficiency.

Panel (f) suggests a weak and inconsistent relationship between Inter-Bead Spacing (IBS) and Hardness (H2). While some negative derivatives appear at lower IBS values, the overall distribution remains scattered, indicating that IBS does not have a strong direct influence on hardness. However, variations in hardness at specific IBS values suggest that its influence is more pronounced in combination

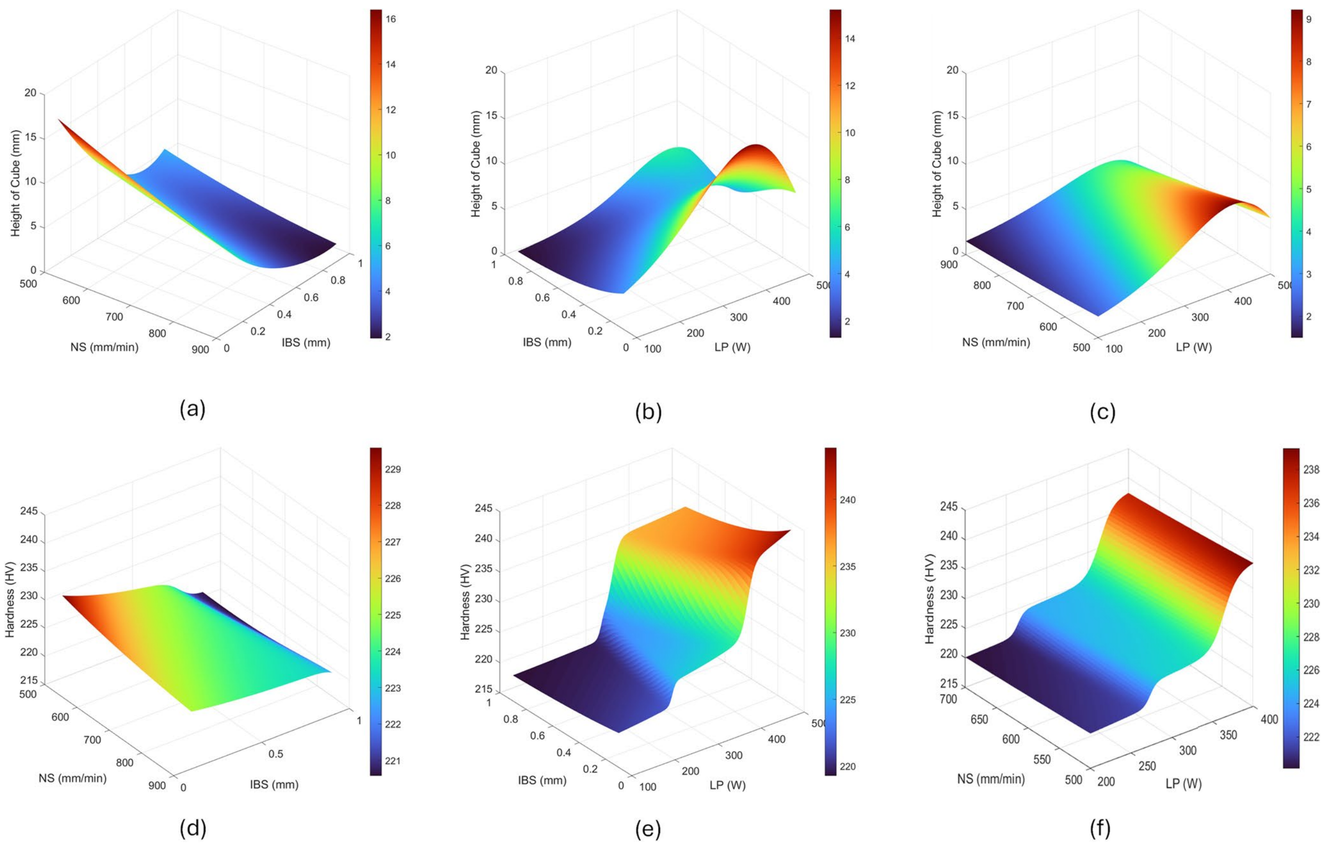

Fig. 25 ANN-predicted response surfaces for Cube fabrication objectives as functions of process parameters. (**a-c**) Height of Cube variations with NS (mm/min), IBS (mm), and LP (W). (**d-f**) Hardness variations with NS (mm/min), IBS (mm), and LP (W)

with LP and NS variations. This suggests that IBS primarily affects material distribution rather than directly influencing densification.

Figure 26 confirms that LP is a key factor affecting both height and hardness, particularly at higher power levels. LP exhibits a nonlinear influence on height, where moderate values enhance deposition but excessive power may introduce variability. NS negatively impacts height by reducing deposition time and also lowers hardness due to reduced energy absorption per unit area. IBS plays a moderate role, primarily influencing height formation, while its effect on hardness remains weak and context-dependent. These findings emphasize the importance of precise LP and NS tuning to optimize both dimensional accuracy and mechanical properties.

The total contribution of each parameter to height and hardness was calculated using Eq. (8). For the height of cube (H1), LP contributes 52.26%, IBS accounts for 41.38%, and NS has a minor effect at 6.35%. For hardness (H2), LP dominates with 96.51%, while IBS (2.98%) and NS (0.42%) have negligible contributions.

These results further confirm that LP has the most significant impact on both height and hardness, while NS plays a minimal role, and IBS is an important secondary factor for height but not hardness. This reinforces the need for precise LP and NS adjustments to achieve optimal process performance.

Bootstrap-based robustness verification and kernel density–based diagnostic distributions of the PaD sensitivities, used to assess variability and ranking stability, are provided in the Supplementary Material.

Weights-Based sensitivity results For the height of cube, LP is the dominant factor with a relative importance of 54.67%, followed by IBS at 33.62%, while NS has the least influence at 11.70% (Eq. (11)). This suggests that LP is the primary driver of height formation, likely due to its impact on energy input and material flow. The notable contribution of IBS indicates its role in layer spacing and material accumulation, whereas NS has a relatively minor effect, suggesting that variations in scanning speed have limited influence on height formation.

For hardness, LP again has the highest contribution at 67.65%, followed by IBS at 22.88%, and NS at 9.47%. The strong influence of LP suggests that hardness is predominantly controlled by heat input, affecting microstructural transformations and material consolidation. The moderate

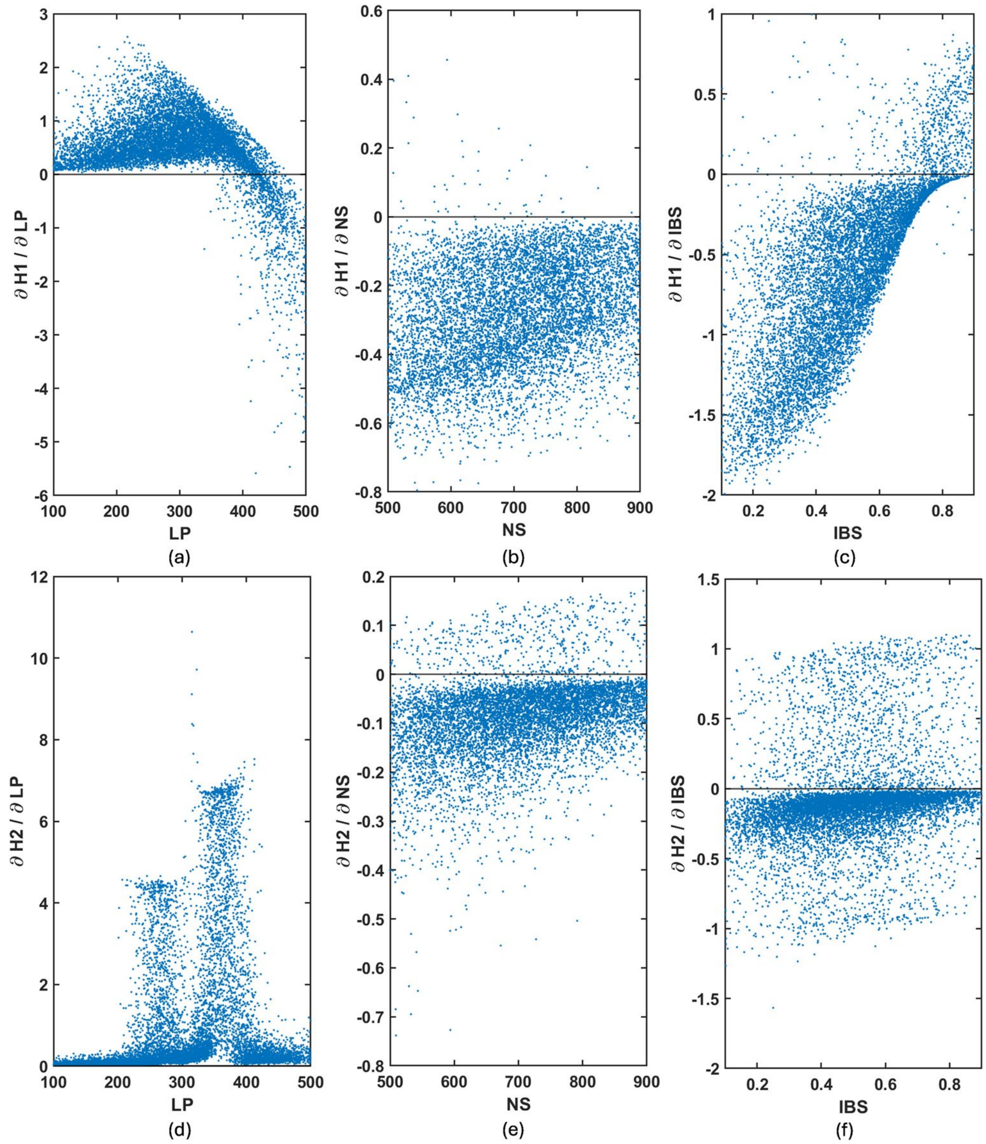

Fig. 26 Partial derivatives of Height of Cube (H1) and Hardness (H2) with respect to Laser Power (LP), Nozzle Speed (NS), and Inter-Bead Distance (IBD): (**a**)–(**c**) Sensitivity of Height of Cube to LP, NS, and IBS. (**d**)–(**f**) Sensitivity of Hardness to LP, NS, and IBS

contribution of IBS indicates that layer spacing affects hardness to some extent, possibly due to changes in deposition uniformity and cooling rates. NS has the lowest influence, suggesting that variations in scanning speed do not significantly affect hardness compared to LP and IBS.

Figure 27a and b present heatmaps of absolute weight magnitudes, visually confirming these findings. The brighter intensity for LP in Fig. 27a (height of cube) highlights its dominant role in height formation, with a secondary but notable contribution from IBS. In Fig. 27b (hardness), the even stronger intensity for LP underscores its primary influence on material hardness, while IBS also contributes meaningfully. The relative weight distributions across neurons further illustrate the nonlinear dependencies, with LP showing the strongest influence across multiple neurons, while IBS plays a moderate role primarily affecting height formation.

Profile method results Figure 28 presents the contribution profiles of Laser Power (LP), Nozzle Speed (NS), and Inter-Bead Spacing (IBS) in determining the height of cube (left) and hardness (right) using the Profile Method at 192 variation intervals. These sensitivity analyses illustrate how variations in each input parameter influence the ANN outputs.

For height of cube, IBS exhibits the highest contribution (~44.98%), showing a decreasing trend as the scale of variation increases. This suggests that inter-bead spacing significantly influences height formation by altering layer deposition and material overlap. LP (~32.40%) follows with a non-monotonic profile, indicating its strong but complex effect on height formation, possibly due to its role in material melting and consolidation. NS (~22.62%) has a moderate influence, showing a relatively stable response, implying a secondary role in determining height of cube.

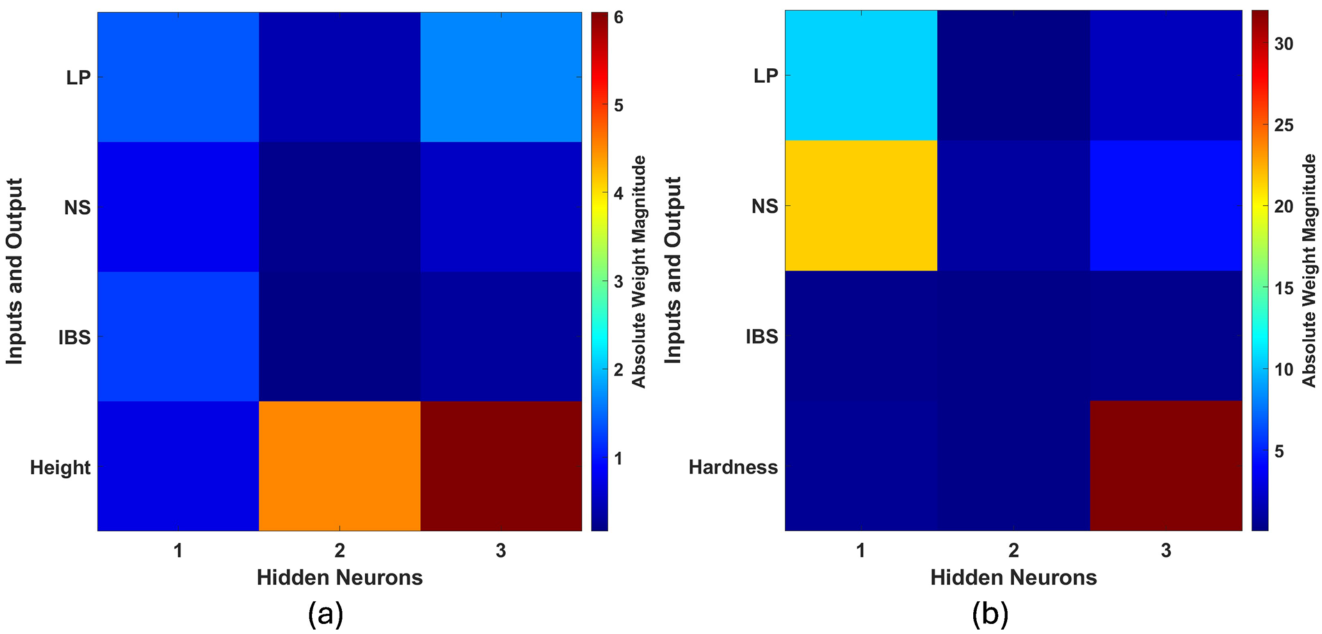

Fig. 27 Heatmaps of absolute weight magnitudes for (**a**) Height of Cube and (**b**) Hardness, illustrating the relative influence of input parameters on ANN predictions. Brighter intensities indicate stronger connections, confirming LP as the dominant factor for both height and hardness, with IBS playing a secondary role

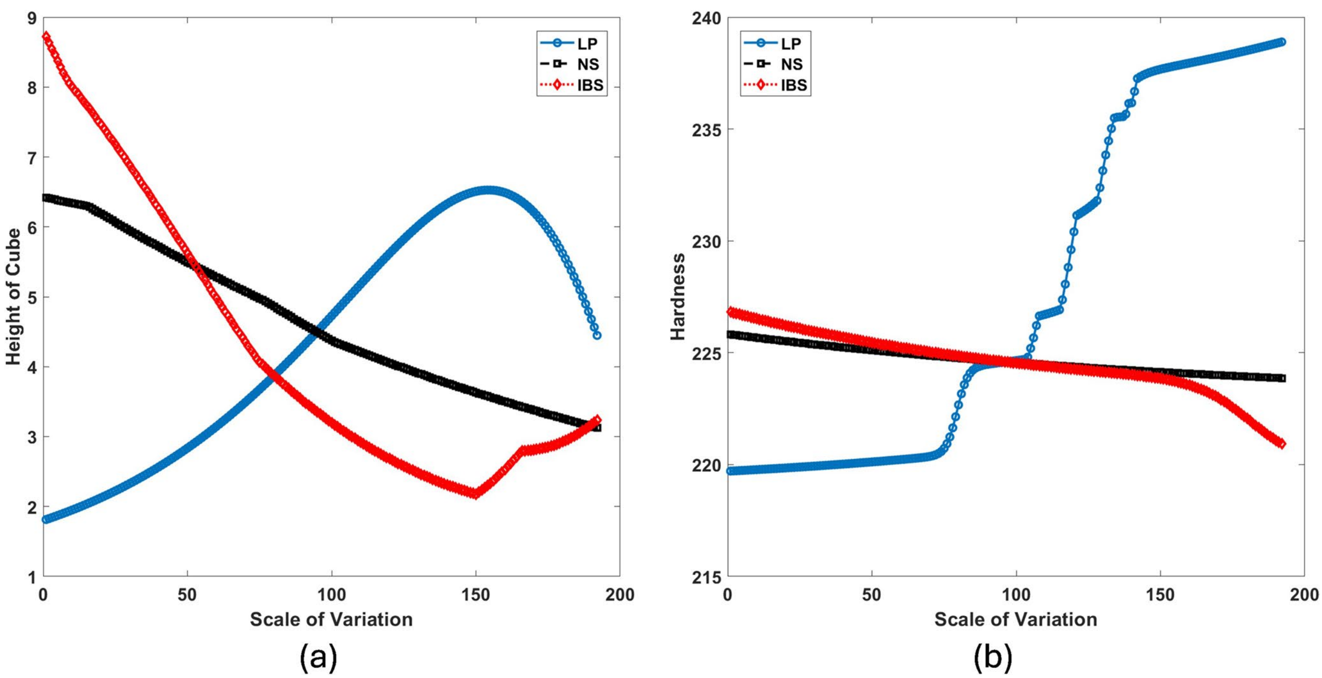

Fig. 28 Influence of Laser Power (LP), Nozzle Speed (NS), and Inter-Bead Spacing (IBS) on (**a**) Height of Cube and (**b**) Hardness using the Profile Method at 192 variation intervals. The results confirm that IBS is the primary contributor to Height of Cube, while LP has the strongest effect on Hardness, with contributions remaining stable across all tested scales

The contributions remained stable across different scales, confirming robustness in sensitivity ranking.

For hardness, LP is the dominant factor (~71.0%), demonstrating a clear increasing trend. This highlights that higher laser power directly enhances hardness due to increased thermal energy and material transformation. IBS (~21.78%) has a moderate but stable influence, suggesting that layer spacing affects cooling rates and material densification, contributing to hardness distribution. NS (~7.22%) contributes the least, indicating that scanning speed has

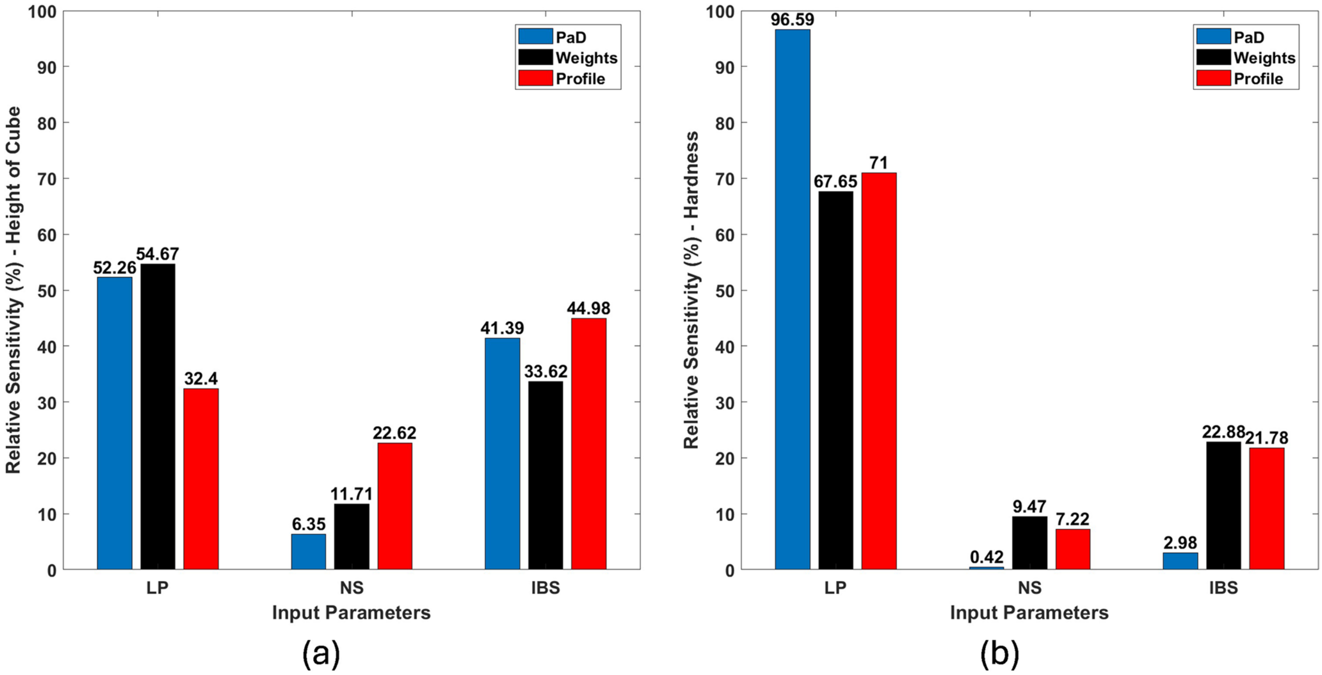

Fig. 29 Comparison of the relative sensitivity of process parameters (Laser Power (LP), Nozzle Speed (NS), and Inter-Bead Spacing (IBS)) in determining (**a**) Height of Cube and (**b**) Hardness, using three different sensitivity analysis methods: Partial Derivative (PaD), Weights-Based, and Profile Method. While all methods consistently rank LP as the dominant factor for Hardness, discrepancies in rankings for Height indicate the influence of broader interaction effects captured by the Profile Method

Table 10 Summary of sensitivity contributions and rankings across methods

Parameter	PaD Method (%)	Weights Method (%)	Profile Method (%)	Average Rank
Height of Cube				
LP	52.26	54.67	32.40	**1.67**
NS	6.35	11.71	22.62	**2.33**
IBS	41.39	33.62	44.98	**2.00**
Hardness				
LP	96.51	67.65	71.00	**1.00**
NS	0.42	9.47	7.22	**3.00**
IBS	2.98	22.88	21.78	**2.00**

minimal impact on hardness compared to LP and IBS. Unlike other outputs, hardness exhibits exceptional stability, with contributions remaining nearly identical across all scales, reinforcing the reliability of the ranking.

Comparative analysis of sensitivity methods To ensure a comprehensive assessment of input parameter influence, three different sensitivity analysis methods were applied: the Partial Derivative (PaD) method, the weights-based method, and the Profile Method. The comparative results for height of cube and hardness are summarized in Fig. 29; Table 10.

Height of Cube Sensitivity The PaD and weights-based methods both identify Laser Power (LP) as the dominant factor, contributing 52.26% and 54.67%, respectively. The Profile Method, however, assigns a much lower contribution to LP (32.40%) and instead ranks Inter-Bead Spacing (IBS) as the most influential factor (44.98%), with Nozzle Speed (NS) following at 22.62%.

This discrepancy in rankings suggests fundamental differences in how each method captures sensitivity:

- This indicates that IBS has a more significant influence when considering global variations, affecting layer accumulation and final part geometry, whereas LP has a stronger instantaneous effect on deposition. This highlights that while LP governs immediate deposition, IBS plays a crucial role in long-term height consistency. The weights-based and PaD methods, which rely on local gradient-based assessments, may not fully capture this broader interaction.
- The nonlinear effects of Nozzle Speed (NS) are more pronounced in the Profile Method, indicating that at certain scales, NS significantly influences height formation by modifying the deposition consistency.

- Methodological Differences: The PaD method captures local sensitivity by evaluating derivative-based contributions, while the weights-based and profile methods account for broader parameter interactions across the entire input space. This is particularly evident in Height of Cube, where interactions between LP, NS, and IBS contribute to nonlinear effects, leading to variations in ranking.

These insights reinforce the necessity of considering multiple sensitivity analysis techniques to gain a comprehensive understanding of parameter influence.

Hardness Sensitivity PaD assigns an overwhelming 96.51% contribution to LP, while the weights-based and profile methods report lower but comparable values (67.65% and 71.00%). This suggests that the PaD method may overestimate local effects due to its derivative-based nature, whereas the Profile Method captures accumulated effects over multiple layers, leading to a more distributed contribution. NS and IBS play minor roles, with NS contributing 0.42% (PaD), 9.47% (weights), and 7.22% (Profile), while IBS remains relatively stable across all methods.

Unlike the case of height, the ranking consistency for hardness across methods reinforces that LP is the primary controlling factor for material hardness, likely due to its direct impact on energy input, thermal diffusion, and solidification kinetics.

Summary of Sensitivity Rankings Despite differences in numerical sensitivity values, the rankings for hardness remain highly consistent across all methods, while Height of Cube exhibits discrepancies in rankings, as shown in Table 10. This variation underscores the importance of considering multiple sensitivity assessment approaches to capture both localized and overall parameter influence.

Table 11 Rank-Correlation summary for cube sensitivity analysis

Objective	Methods Compared	Spearman ρ	Kendall τ	Rank Ordering
Height of Cube	PaD vs. Weights	1.000	1.000	LP > IBS > NS
	PaD vs. Profile	0.500	0.333	PaD: LP > IBS > NS; Profile: IBS > LP > NS
	Weights vs. Profile	0.500	0.333	Weights: LP > IBS > NS; Profile: IBS > LP > NS
Hardness	PaD vs. Weights	1.000	1.000	LP > IBS > NS
	PaD vs. Profile	1.000	1.000	LP > IBS > NS
	Weights vs. Profile	1.000	1.000	LP > IBS > NS

Rank-Correlation Analysis Across Sensitivity Methods To further assess the robustness of the sensitivity analysis for cube fabrication, Spearman's rank correlation coefficient (ρ) and Kendall's coefficient (τ) were computed to quantify agreement among the three methods (PaD, weights-based, and profile). As with the single-bead study, these non-parametric metrics provide a rigorous measure of whether the parameter hierarchy is preserved across fundamentally different sensitivity definitions.

For the Height of Cube objective, the three sensitivity methods do not yield identical rankings. Both the PaD and weights-based analyses rank the parameters as LP → IBS → NS, whereas the Profile Method—reflecting global variations across the entire processing window—ranks them as IBS → LP → NS. This mismatch results in moderate rank correlations, with Spearman's $\rho = 0.500$ and Kendall's $\tau = 0.333$ when comparing either PaD or weights with the Profile Method, while PaD vs. weights show perfect agreement ($\rho = 1.000$, $\tau = 1.000$). The divergence between LP and IBS is physically meaningful: gradient-based approaches emphasize the influence of LP on instantaneous bead height formation, whereas the Profile Method captures cumulative, multi-layer effects for which IBS becomes the dominant geometrical regulator of overall build height. Thus, the moderate correlation reflects a genuine shift between local melt-pool dynamics and global layer-stacking behavior rather than methodological inconsistency.

For Hardness, all three methods produce identical rankings (LP → IBS → NS), yielding perfect agreement across all correlations ($\rho = 1.000$; $\tau = 1.000$). This strong consistency reflects the fact that hardness is primarily governed by laser power through its effect on melt-pool thermal history, cooling rate, and solidification kinetics, whereas IBS and NS contribute only secondary thermal modulation.

The complete rank-correlation matrix for cube fabrication is shown in Table 11.

Interpretation and Physical Justification The differences observed in the height-of-cube rankings arise naturally from the fact that height formation is governed by multiscale mechanisms acting across the entire layer-stacking process rather than by instantaneous melt-pool behavior. Gradient-based approaches such as PaD and the weights-based method emphasize local deposition effects and therefore identify Laser Power (LP) as the most influential factor, because LP directly determines the height of each newly deposited bead. In contrast, the Profile Method explores broader, global variations across the full input space and captures cumulative interactions between layers. Under these global conditions, Inter-Bead Spacing (IBS) becomes more dominant because it regulates geometric accumulation over many layers, influencing layer overlap, stair-stepping behavior, thermal smoothing, and the extent to which successive tracks reinforce or diminish overall build height. The moderate rank correlations ($\rho = 0.5$, $\tau = 0.33$) therefore do not indicate inconsistency, but rather reflect the expected shift in dominant mechanisms when transitioning from local melt-pool dynamics to global geometric growth.

For hardness, all three sensitivity methods yield identical rankings, which is fully consistent with its physical origin. Hardness depends primarily on the thermal history of the melt pool—particularly energy input and cooling rate—both of which are overwhelmingly controlled by LP. IBS and NS influence hardness only indirectly by modulating secondary thermal effects, and their impact remains comparatively small. Because hardness varies within a narrower range and is governed by a single dominant mechanism, all methods converge to the same parameter hierarchy, producing perfect rank agreement ($\rho = 1.0$, $\tau = 1.0$).

This cross-method analysis demonstrates that the ANN-based framework produces highly stable sensitivity rankings for hardness, and physically interpretable yet scale-dependent rankings for cube height. The perfect agreement for hardness confirms that LP is unequivocally the dominant factor governing melt-pool thermodynamics and microstructural consolidation. For height, the differing rankings arise because local-gradient methods emphasize instantaneous deposition dynamics, while the Profile Method captures long-range geometric accumulation effects and therefore prioritizes IBS. The combination of strong agreement where expected (hardness) and physically justified divergence where multi-scale effects dominate (height) reinforces the validity of using multiple complementary sensitivity techniques to obtain a complete and robust understanding of parameter influence in DED cube fabrication.

4.2.4 Multi-objective optimization

The NSGA-II optimization produced a Pareto front that describes the trade-off between cube height and hardness. A complete view of the optimization behaviour is shown through the convergence history (Fig. 30a), the multi-run stability analysis (Fig. 30b), and the final Pareto front with the selected solution (Fig. 30c). In contrast to the single-bead case, both objectives exhibit a positively correlated trend, where increasing the height of the cube generally leads to a slight increase in hardness. This reflects the influence of thermal history and layer stacking on microstructural consolidation.

For the cube optimization, explicit normalization was likewise not applied. Although the objectives differ in physical units (mm for height and HV for hardness), their numerical ranges are comparable and tightly bounded within the experimental domain. As a result, Pareto dominance is not influenced by unit scaling, and the NSGA-II solver evaluates trade-offs consistently without normalization. The robustness of this formulation is further supported by the strong overlap of Pareto fronts obtained from multiple independent optimization runs.

Since the cube geometry was constrained to remain close to 5 mm, as defined in Eq. (16), the final selection was made along the upper region of the Pareto front to balance dimensional accuracy with mechanical performance, ensuring adequate hardness without excessive overbuilding.

To ensure reliable convergence and thorough exploration of the design space, MATLAB's *gamultiobj* solver was configured using the parameters listed in Table 12. These settings follow standard NSGA-II recommendations for low-dimensional nonlinear multi-objective systems.

NSGA-II convergence was assessed using the Pareto spread metric, which evaluates the distribution of non-dominated solutions. As shown in Fig. 30a, the spread decreases rapidly during the early generations and then stabilizes, indicating consistent convergence toward a narrow objective region. Because both cube objectives vary within a very tight range, only minimal spread remains at convergence—consistent with the expected physical response characteristics.

To verify robustness and rule out sensitivity to random initialization, the optimization was repeated five times with different random seeds. The resulting Pareto fronts in Fig. 30b overlap almost entirely, confirming high run-to-run repeatability. The small deviation of one point is expected given the extremely narrow objective window (height variation < 0.3 mm and hardness variation < 0.3 HV), and does not affect the identification of the optimal solution.

The final optimized parameters and corresponding model predictions are summarized in Table 13, alongside experimental validation results.

This optimization confirms that the ANN–NSGA-II framework effectively balances geometric accuracy and mechanical performance for cube fabrication. The very low prediction errors—0.271% for height and 0.810% for hardness—demonstrate strong predictive reliability and reinforce the suitability of the approach for broader additive manufacturing design and process optimization.

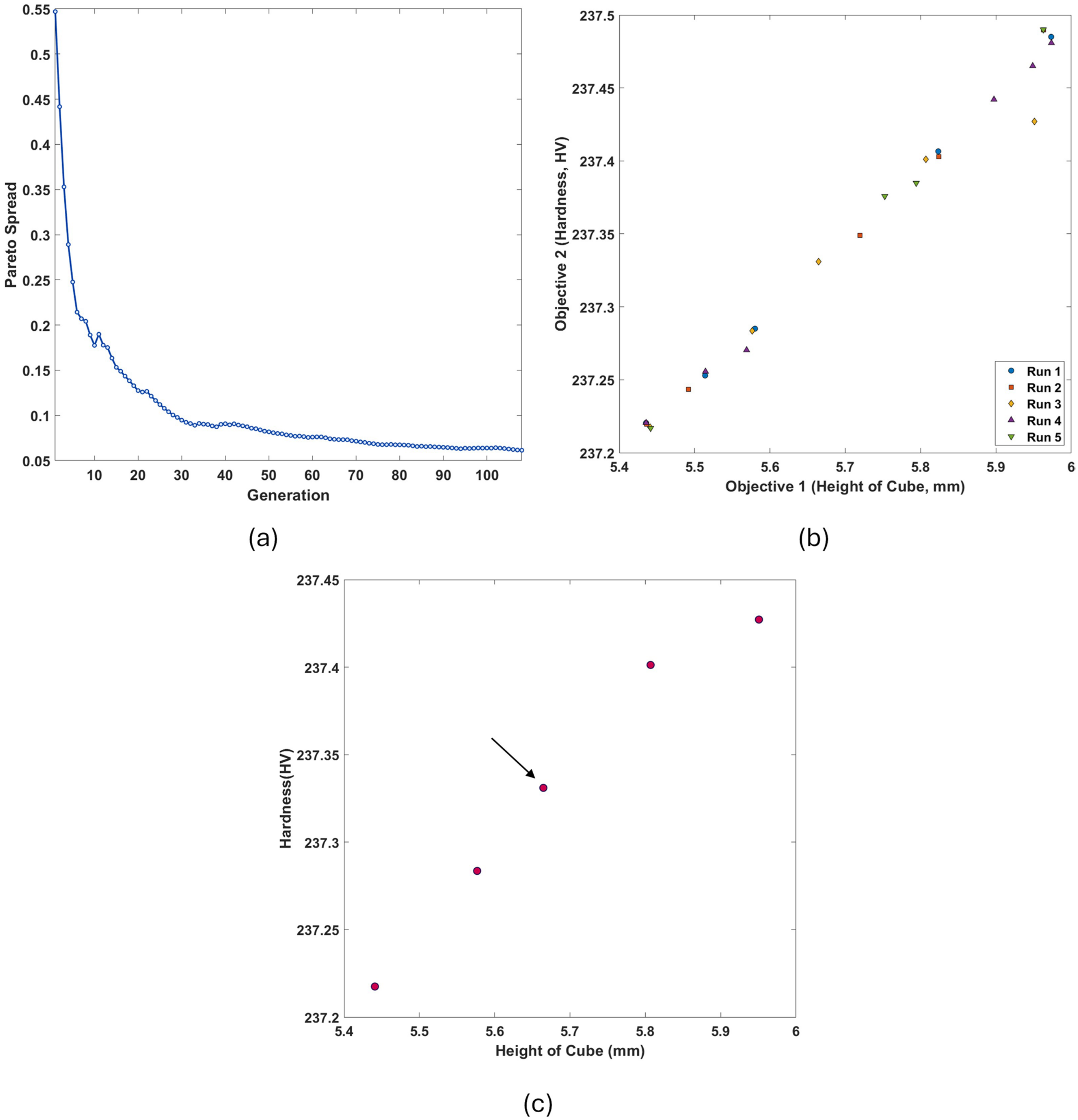

Fig. 30 (**a**) NSGA-II convergence curve for cube optimization. (**b**) Stability of NSGA-II Pareto fronts across five independent runs. The fronts overlap closely, with only minor variation attributable to stochastic sampling within a narrow objective range. (**c**) Final Pareto front and selected solution for cube fabrication

5 Conclusion

This study developed and validated a modular, machine learning-driven optimization framework for laser-based Directed Energy Deposition (DED), combining artificial neural network (ANN) surrogate modeling, NSGA-II multi-objective optimization, and sensitivity analysis to evaluate parameter influence. The framework was experimentally demonstrated on two case studies: single-bead and cube fabrication.

In the single-bead study, the framework effectively balanced bead width and dilution depth. Laser power and feed rate emerged as dominant factors, and the ANN model achieved high accuracy, with prediction errors of 1.28%

Table 12 NSGA-II configuration used in cube optimization

Parameter	Value
Population size	50
Pareto fraction	0.10
Crossover fraction	0.80
Crossover function	Intermediate (ratio = 1.0)
Mutation	Adaptive (default)
Migration	Forward, 0.20 fraction
Maximum generations	200
Stall generations	100
Function tolerance	1×10^{-4}
Constraint tolerance	1×10^{-3}
Stopping criterion	Average change in Pareto spread below tolerance
Number of independent runs	5 (for stability analysis)

Table 13 Overall optimization summary for cube fabrication

Parameter/Objective	Value
Laser Power (W)	485.314 (485)
Feed Rate or Nozzle Speed (mm/min)	656.783 (657)
Inter-Bead Spacing (mm)	0.771 (0.8)
Predicted Height of Cube (mm)	5.665
Experimental Height of Cube (mm)	5.68
Height of Cube prediction error (%)	0.271
Predicted Hardness (HV)	237.331
Experimental Hardness (HV)	239.27
Hardness prediction error (%)	0.810

for dilution and 4.11% for width. NSGA-II optimization yielded a clear Pareto front, offering multiple parameter sets tailored to competing objectives.

In the cube fabrication case, the framework optimized build height and surface hardness with prediction errors of 0.271% and 0.810%, respectively. Sensitivity analysis confirmed that inter-bead spacing and laser power were the most influential parameters, supporting model reliability in complex scenarios.

By integrating data-driven prediction, multi-objective optimization, and sensitivity-guided insight, the proposed framework supports efficient, flexible process planning. Its generalizable structure allows extension beyond DED to other additive and subtractive manufacturing methods requiring simultaneous control over multiple quality metrics. While both case studies use Inconel 718 deposited on stainless steel, the framework is adaptable to other material systems through retraining and tailored data collection.

Overall, this work demonstrates that combining surrogate modeling with evolutionary optimization and parameter influence analysis can significantly reduce experimental effort, improve manufacturing efficiency, and offer practical benefits for industrial implementation.

Supplementary Information The online version contains supplementary material available at https://doi.org/10.1007/s00170-026-17560-5.

Author contributions Parviz Kahhal contributed to the conceptualization, methodology, software development, visualization, project administration, supervision, and wrote the original draft. Hong Seok Kim was responsible for formal analysis, data curation, project administration, and visualization. Mahmoud Moradi contributed to investigation, formal analysis, and writing—review and editing. Sang-Hu Park contributed to conceptualization, resource provision, supervision, funding acquisition, and writing—review and editing. All authors read and approved the final manuscript.

Funding Open Access funding enabled and organized by CAUL and its Member Institutions. This work is supported by Korea Basic Science Institute (National research Facilities and Equipment Center) grant funded by the Ministry of Education (No. 2021R1A6C101A449), and also supported by the National Research Foundation of Korea (NRF) (No. RS-2023-NR076859).

Declarations

Competing interests The authors have no relevant financial or non-financial interests to disclose.

References

1. Svetlizky D et al (2021) Directed energy deposition (DED) additive manufacturing: physical characteristics, defects, challenges and applications. Mater Today 49:271–295
2. Kanishka K, Acherjee B (2023) Revolutionizing manufacturing: a comprehensive overview of additive manufacturing processes, materials, developments, and challenges. J Manuf Process 107:574–619
3. Li Z et al (2022) High deposition rate powder-and wire-based laser directed energy deposition of metallic materials: A review. Int J Mach Tools Manuf 181:103942
4. Kim TG, Shim DS (2021) Effect of laser power and powder feed rate on interfacial crack and mechanical/microstructural characterizations in repairing of 630 stainless steel using direct energy deposition. Mater Sci Eng A 828:142004
5. Kahhal P, Jo Y-K, Park S-H (2024) Recent progress in remanufacturing technologies using metal additive manufacturing processes and surface treatment. Int J Precis Eng Manuf-Green Technol 11:625–658. https://doi.org/10.1007/s40684-023-00551-2
6. Ghanavati R et al (2023) Residual stresses and distortion in additively-manufactured SS316L-IN718 multi-material by laser-directed energy deposition: A validated numerical-statistical approach. J Manuf Process 108:292–309

7. Choi JW et al (2022) Sequential process optimization for a digital light processing system to minimize trial and error. Sci Rep 12(1):13553. https://doi.org/10.1038/s41598-022-17841-5
8. Chia HY et al (2022) Process parameter optimization of metal additive manufacturing: A review and outlook. J Mater Inf 2(4). https://doi.org/10.20517/jmi.2022.18
9. Sarkar D, Kapil A, Sharma A (2024) Advances in computational modeling for laser powder bed fusion additive manufacturing: a comprehensive review of finite element techniques and strategies. Addit Manuf. https://doi.org/10.1016/j.addma.2024.104157
10. Francois MM et al (2017) Modeling of additive manufacturing processes for metals: challenges and opportunities. Curr Opin Solid State Mater Sci 21(4):198–206. https://doi.org/10.1016/j.cossms.2016.12.001
11. Wang C et al (2020) Machine learning in additive manufacturing: State-of-the-art and perspectives. Additive Manuf 36:101538
12. Qin J et al (2022) Research and application of machine learning for additive manufacturing. Additive Manuf 52:102691
13. Sondagar H, Bhadauria S, Sharma V (2021) *Artificial neural network (ANN) based prediction of process parameters in additive manufacturing*. in *IOP Conf. Ser.: Mater. Sci. Eng.* IOP Publishing
14. Shirmohammadi M, Goushchi SJ, Keshtiban PM (2021) Optimization of 3D printing process parameters to minimize surface roughness with hybrid artificial neural network model and particle swarm algorithm. Prog Addit Manuf 6(2):199–215. https://doi.org/10.1007/s40964-021-00166-6
15. Malakooti BB, Zhou YQ, Tandler EC (1995) -process regressions and adaptive multicriteria neural networks for monitoring and supervising machining operations. J Intell Manuf 6:53–66
16. Le VT et al (2023) Efficient prediction of thermal history in wire and Arc additive manufacturing combining machine learning and numerical simulation. Int J Adv Manuf Technol 126(9):4651–4663. https://doi.org/10.1007/s00170-023-11473-3
17. Chowdhury S, Anand S (2016) *Artificial neural network based geometric compensation for thermal deformation in additive manufacturing processes*. in *Int. Manuf. Sci. Eng. Conf.* American Society of Mechanical Engineers
18. Nguyen PD, Dao MB, Nguyen TQ (2025) AI-driven optimization in 3D printing: reducing time and material consumption through machine learning models. Mater Emerg Technol Sustain 01(01):2450001. https://doi.org/10.1142/s3060932124500018
19. Phuong Dong N et al (2022) A data-driven machine learning approach for the 3D printing process optimisation. Virtual Phys Prototyp 17(4):768–786. https://doi.org/10.1080/17452759.2022.2068446
20. Yakubu Adekunle A et al (2024) Optimization of 4D/3D printing via machine learning: A systematic review. Hybrid Adv 6:100242. https://doi.org/10.1016/j.hybadv.2024.100242
21. Altun F et al (2025) AI-Driven innovations in 3D printing: Optimization, Automation, and intelligent control. J Manuf Mater Process 9(10):329
22. Gevrey M, Dimopoulos I, Lek S (2003) Review and comparison of methods to study the contribution of variables in artificial neural network models. Ecol Model 160(3):249–264
23. Kadhim ZS, Abdullah HS, Ghathwan KI (2022) Artificial Neural Network Hyperparameters Optimization: A Survey. International Journal of Online and Biomedical Engineering (iJOE). https://doi.org/10.3991/ijoe.v18i15.34399
24. Jabbar H, Khan RZ (2015) *Methods to avoid over-fitting and under-fitting in supervised machine learning (comparative study).* Computer Science, Communication and Instrumentation Devices, 70(10.3850): pp. 978–981.https://doi.org/10.3850/978-981-09-5247-1_017
25. Gao S, Yue X, Wang H (2024) Predictability of different machine learning approaches on the fatigue life of additive-manufactured porous titanium structure. Metals 14(3):320
26. Kahhal P et al (2022) Neural Network-Based Multi-Objective optimization of adjustable drawbead movement for deep drawing of Tailor-Welded blanks. Mater 15(4):1430. https://doi.org/10.3390/ma15041430
27. Mehrabi O, Seyedkashi SH, Moradi M (2023) Experimental and response surface study on additive manufacturing of functionally graded steel-inconel wall using direct laser metal deposition. Opt Laser Technol 167:109707
28. Mohamed OA, Masood SH, Bhowmik JL (2015) Optimization of fused deposition modeling process parameters: a review of current research and future prospects. Adv Manuf 3:42–53
29. Inman E et al (2025) Stronger, lighter, and faster: multi-objective bayesian optimization for fused filament fabrication. Progress Additive Manuf 10(4):2601–2611. https://doi.org/10.1007/s40964-024-00769-9
30. Deb K et al (2002) A fast and elitist multiobjective genetic algorithm: NSGA-II. IEEE Trans Evol Comput 6(2):182–197. https://doi.org/10.1109/4235.996017
31. Asadollahi-Yazdi E, Gardan J, Lafon P (2018) Multi-objective optimization of additive manufacturing process. IFAC-PapersOnLine 51(11):152–157. https://doi.org/10.1016/j.ifacol.2018.08.250
32. Yang J et al (2024) Prediction-based multi-objective optimization method for 3D printing resource consumption. Int J Adv Manuf Technol 134(3):1805–1843. https://doi.org/10.1007/s00170-024-14143-0
33. Ma H et al (2023) A comprehensive survey on NSGA-II for multi-objective optimization and applications. Artif Intell Rev 56(12):15217–15270
34. Patil P et al (2021) Multi-objective optimization of process parameters of fused deposition modeling (FDM) for printing polylactic acid (PLA) polymer components. Mater Today Proc 45:4880–4885
35. Wang G et al (2024) Multi-objective optimisation of process parameters for laser-based directed energy deposition of a mixture of H13 and M2 steel powders on 4Cr5Mo2SiV1 steel. Virtual Phys Prototyp 19(1):e2290184
36. Liu A et al (2024) A multi-objective optimization method of directed energy deposition manufacturing process considering carbon emission. J Clean Prod. https://doi.org/10.1016/j.jclepro.2024.142144
37. Chang Y-Y, Qiu J-R, Hwang S-J (2022) Multi-objective optimization of directed energy deposition process by using Taguchi-Grey relational analysis. Int J Adv Manuf Technol 120(11):7547–7563. https://doi.org/10.1007/s00170-022-09210-3
38. Li J et al (2024) Multi-Objective optimization of process parameters in laser DED Ni-Based powder on steel rail using response surface design. Coatings 14(4):401
39. Trivedi A, Patel M (2025) Multi-objective optimization of material extrusion additively manufactured parts from PETG feedstock material using grey wolf algorithm. Prog Addit Manuf 10(5):3807–3825. https://doi.org/10.1007/s40964-024-00839-y
40. Moradi M et al (2022) Direct laser metal deposition (DLMD) additive manufacturing (AM) of inconel 718 superalloy: Elemental, microstructural and physical properties evaluation. Optik 259:169018. https://doi.org/10.1016/j.ijleo.2022.169018
41. Montgomery DC (2017) Design and analysis of experiments. John wiley & sons
42. Santner TJ et al (2018) Space-filling designs for computer experiments. Springer
43. Kahhal P et al (2023) Metaheuristic optimization of powder size distribution in powder forming process using Multi-Particle finite element method coupled with artificial neural network and genetic algorithm. Mater Trans 64(11):2648–2655. https://doi.org/10.2320/matertrans.MT-MI2022006

44. Uzair M, Jamil N *Effects of hidden layers on the efficiency of neural networks*. in (2020) *IEEE 23rd international multitopic conference (INMIC)*. 2020. IEEE
45. Hiroyasu T et al (2002) Multi-objective optimization of diesel engine emissions and fuel economy using genetic algorithms and phenomenological model. SAE Technical Paper
46. Talbi E (2009) Metaheuristics: From Design to Implementation, vol 2. John Wiley & Sons, pp 268–308
47. Yang X-S (2014) Nature-Inspired Optimization Algorithms. Elsevier, London
48. Kahhal P, Brooghani SYA, Azodi HD (2013) Multi-objective optimization of sheet metal forming die using FEA coupled with RSM. J Mech Sci Technol 27:3835–3842. https://doi.org/10.1007/s12206-013-0927-8
49. Goldberg DE (2013) Genetic algorithms. pearson education India
50. Konak A, Coit DW, Smith AE (2006) Multi-objective optimization using genetic algorithms: a tutorial. Reliab Eng Syst Saf 91(9):992–1007
51. Deb K (2011) Multi-objective optimisation using evolutionary algorithms: an introduction. Multi-objective evolutionary optimisation for product design and manufacturing. Springer, pp 3–34
52. Nourani V, Sayyah M, Fard (2012) Sensitivity analysis of the artificial neural network outputs in simulation of the evaporation process at different climatologic regimes. Adv Eng Softw 47(1):127–146. https://doi.org/10.1016/j.advengsoft.2011.12.014
53. Goh AT (1995) Back-propagation neural networks for modeling complex systems. Artif Intell Eng 9(3):143–151. https://doi.org/10.1016/0954-1810(94)00011-S
54. Lek S et al (1996) Application of neural networks to modelling nonlinear relationships in ecology. Ecol Model 90(1):39–52
55. Zwillinger D, Kokoska S (1999) CRC standard probability and statistics tables and formulae. Crc
56. Agresti A (2010) Analysis of ordinal categorical data. John Wiley & Sons
57. Jo Y-K et al (2023) Higher wear-resistant surfacing at high temperatures using a hybrid cladding process. Mater Des 225:111553. https://doi.org/10.1016/j.matdes.2022.111553
58. Manufacturing SA (2024) *Osprey® 718 Metal Powder Datasheet*
59. Fathi A et al (2006) Prediction of melt pool depth and Dilution in laser powder deposition. J Phys D 39(12):2613. https://doi.org/10.1088/0022-3727/39/12/022